JACS
JOURNAL OF THE AMERICAN CHEMICAL SOCIETY

Subscriber access provided by KUNGL TEKNISKA HOGSKOLAN

Article

Nature of Activated Manganese Oxide for Oxygen Evolution

Michael Huynh, Chenyang Shi, Simon J. L. Billinge, and Daniel G. Nocera

J. Am. Chem. Soc., **Just Accepted Manuscript** • DOI: 10.1021/jacs.5b06382 • Publication Date (Web): 02 Nov 2015

Downloaded from http://pubs.acs.org on November 3, 2015

Just Accepted

"Just Accepted" manuscripts have been peer-reviewed and accepted for publication. They are posted online prior to technical editing, formatting for publication and author proofing. The American Chemical Society provides "Just Accepted" as a free service to the research community to expedite the dissemination of scientific material as soon as possible after acceptance. "Just Accepted" manuscripts appear in full in PDF format accompanied by an HTML abstract. "Just Accepted" manuscripts have been fully peer reviewed, but should not be considered the official version of record. They are accessible to all readers and citable by the Digital Object Identifier (DOI®). "Just Accepted" is an optional service offered to authors. Therefore, the "Just Accepted" Web site may not include all articles that will be published in the journal. After a manuscript is technically edited and formatted, it will be removed from the "Just Accepted" Web site and published as an ASAP article. Note that technical editing may introduce minor changes to the manuscript text and/or graphics which could affect content, and all legal disclaimers and ethical guidelines that apply to the journal pertain. ACS cannot be held responsible for errors or consequences arising from the use of information contained in these "Just Accepted" manuscripts.

ACS Publications

Journal of the American Chemical Society is published by the American Chemical Society. 1155 Sixteenth Street N.W., Washington, DC 20036
Published by American Chemical Society. Copyright © American Chemical Society. However, no copyright claim is made to original U.S. Government works, or works produced by employees of any Commonwealth realm Crown government in the course of their duties.

Nature of Activated Manganese Oxide for Oxygen Evolution

Michael Huynh,[a] Chenyang Shi,[b] Simon J. L. Billinge,[b,c] Daniel G. Nocera*,[a]

[a]Department of Chemistry and Chemical Biology, Harvard University, Cambridge, Massachusetts 02138. [b]Department of Applied Physics and Applied Mathematics, Columbia University, New York, New York 10027. [c]Condensed Matter Physics and Materials Science Department, Brookhaven National Laboratory, Upton, New York 11973.

Supporting Information

ABSTRACT: Electrodeposited manganese oxide films (MnOx) are promising stable oxygen evolution catalysts. They are able to catalyze the oxygen evolution reaction in acidic solutions but with only modest activity when prepared by constant anodic potential deposition. We now show that the performance of these catalysts is improved when they are "activated" by potential cycling protocols, as measured by Tafel analysis (where lower slope is better): upon activation the Tafel slope decreases from ~120 mV/decade to ~70 mV/decade in neutral conditions and from ~650 mV/decade to ~90 mV/decade in acidic solutions. Electrochemical, spectroscopic, and structural methods were employed to study the activation process and support a mechanism where the original birnessite-like MnOx (δ-MnO_2) undergoes a phase change, induced by comproportionation with cathodically generated $Mn(OH)_2$, to a hausmannite-like intermediate (α-Mn_3O_4). Subsequent anodic conditioning from voltage cycling or water oxidation produces a disordered birnessite-like phase, which is highly active for oxygen evolution. At pH 2.5, the current density of activated MnOx (at an overpotential of 600 mV) is two orders of magnitude higher than that of the original MnOx and begins to approach that of Ru and Ir oxides in acid.

INTRODUCTION

A logical and sustainable response to the drastic growth in global energy needs is the use solar energy for the production of inexpensive, scalable, sustainable and carbon-neutral fuels.[1–6] Central to this process is the photoelectrochemical (PEC) driven splitting of water to oxygen and hydrogen.[5–10] We have championed buried junction devices for PEC water splitting where catalysts are interfaced to semiconductors such as silicon via conducting interfaces[11–13] and shown these constructs to capture many of the basic functional elements of photosynthesis.[14,15] An advantage of the buried junction is that the light absorber and catalyst may be independently optimized.[16,17] This approach is generally being adopted by others[18,19] with the emphasis that the construction of a system requires both the photoelectrode and catalysts to be active and stable under a given electrolyte environment.[13,20–22] In particular, the development of the photoanode is difficult because popular photovoltaic materials (such as silicon) are more stable in acidic pH,[22–25] while active and abundant oxygen evolution catalysts (OECs), such as oxidic cobalt and nickel films, operate best in neutral to alkaline conditions and quickly corrode at lower pH regimes.[26–32] We have addressed this challenge by developing an acid stable OEC based on an electrodeposited manganese oxide (MnOx).[33,34] By exploiting the intrinsic strength of the manganese–oxygen bond as well as the self-healing nature of MnOx, oxygen evolution in highly acidic electrolytes was demonstrated without degradation of the catalyst.[34] However, the low activity of MnOx in acid precluded its practical applicability as an earth-abundant alternative to Ru and Ir oxides, the only known active and acid stable OECs.[35–42]

Thus, we turned our attention to increasing the oxygen evolution reaction (OER) activity of MnOx. Recent literature suggests that the method of deposition can affect catalytic activity as manganese oxides have been studied extensively in neutral to alkaline conditions[43–56] and, to a lesser extent, acidic solutions,[34,54–59] yet their reported performance vary. Dau et al.[47] and Jaramillo et al.[49] reported that deposition via cyclic voltammetry (CV) results in more active manganese oxide films (in neutral and alkaline electrolyte) than those prepared at constant potential. They proposed that CV deposition introduces more Mn^{3+} valency in the oxide that promotes turnover. This perspective is shared by Dismukes et al. where they evaluated a variety of chemically-prepared manganese oxide polymorphs and discovered that oxides containing more Mn^{3+} and Mn^{2+} exhibited the highest OER activities.[48]

Motivated by these results, we suspected the ability to access different compositions and polymorphs by electrochemical means (e.g., a Pourbaix diagram of Mn[25]) could explain the increased activity of samples deposited by voltage cycling. We now elucidate the conditions necessary for activating MnOx and correlate functional changes with structural transformations. The activation process begins with a phase change driven by the comproportionation of the original birnessite-like (δ-MnO_2) film with cathodically generated $Mn(OH)_2$ to produce a hausmannite-like (α-Mn_3O_4) intermediate. Subsequent anodic conditioning during voltage cycling or oxygen evolution produces activated MnOx, which is active towards OER and exhibits low Tafel slopes of ~70 mV/decade in neutral pH (originally ~120 mV/decade) and ~90 mV/decade under acidic conditions (originally ~650 mV/decade). X-ray pair distribution function (PDF) analysis of these activated MnOx films reveals that the anodic conditioning results in a transformation of hausmannite back to birnessite but as a disordered phase, which is the active OER catalyst. In phosphate (P_i) buffer at pH 2.5, the activated MnOx exhibits current densities (1 mA/cm^2) that are two orders of magnitude greater than the original film when operated at an overpotential of 600 mV. These results represent a path towards

ACS Paragon Plus Environment

replacing precious Ru and Ir oxides for oxygen evolution in acidic environments with oxide-based catalysts comprising non-critical materials.

EXPERIMENTAL SECTION

General electrochemical details. All electrochemical experiments (unless otherwise specified) employed a CH Instruments 760D potentiostat in a three-electrode configuration with a porous glass frit separating the working and auxiliary compartments of the glass H-cell. Glassware was cleaned by soaking in aqua regia and rinsing with type I reagent water (EMD Millipore, 18 MΩ cm resistivity). Fluorine-doped, tin oxide-coated glass (FTO) with 7 Ω/sq surface resistivity (TEC-7, precut 1 cm × 2.5 cm slides from Hartford Glass) was used as the working electrode. FTO slides were sonicated in acetone and rinsed with type I water before use. A 1 cm^2 geometric electrode area was created by masking the FTO with Scotch tape. An Ag/AgCl reference electrode (BASi, filled with saturated KCl) and a Pt mesh (99.9%, Alfa Aesar) auxiliary electrode completed the setup. All experiments were conducted at ambient temperature (~23 °C) and employed automatic *iR* compensation where the electrode and solution resistance was determined by applying a small potential step at the open circuit potential. Potentials were converted to the NHE scale by the following relation: $E_{NHE} = E_{Ag/AgCl} + 0.197$ V, and overpotentials (η) for the oxygen evolution reaction from water were calculated by: $\eta = E_{NHE} - (1.23\ V - 0.059\ V \times pH)$.

Methods for film electrodeposition. MnOx catalyst films were prepared with varying electrodeposition protocols in solutions containing 0.5 mM Mn^{2+} (prepared from $MnCl_2 \cdot 4H_2O$, 99.995% trace metal basis, Strem) and 0.9 M KNO_3 (99.0–100.5%, Macron), unless otherwise specified. All films were then briefly immersed in type I water to remove any trace Mn^{2+}, and any subsequent electrochemical characterization was performed immediately to prevent films from drying. All deposition protocols were adjusted to obtain similar mass loadings of the catalyst films by using a QCM.

The first method for MnOx deposition was at constant potential, where 1.1 V (vs. NHE unless otherwise specified) was applied to the electrode for 600 s. MnOx was also deposited at constant potential in the presence of buffer using procedures described previously:[33] 0.54 V potential at the electrode immersed in 0.5 mM Mn^{2+}, 50 mM methylphosphonate (MeP_i), and 0.9 M KNO_3 at pH 8.0. The second deposition method was by CV: the electrode was cycled 25 times between a potential of 1.7 to –0.8 V at a scan rate of 100 mV/s. A sample was also prepared via CV deposition without the presence of KNO_3 supporting electrolyte. The third approach for preparing MnOx films was by multipotential (MP) steps, where the electrode was initially held at 1.1 V for 3 s, followed by –0.4 V for 2 s and repeated 50 times. The potential and duration of each pulse was varied to determine the optimal conditions for catalyst formation. Multipotential deposition was also performed in MeP_i buffer as a control. The fourth technique for MnOx deposition is called cathodization, where a pre-existing MnOx film deposited at constant anodic potential (described earlier) is subjected to a potential of –0.4 V for 2000 s. Finally, the fifth method for producing MnOx is by purely cathodic deposition, where the electrode was poised at –0.4 V for 2000 s. A variation in cathodic deposition employed a short anodic pulse of 1.0 V for 30 s following the end of the cathodic pulse.

Tafel data collection. The OER activity of MnOx films was evaluated by collecting steady-state current density (j) as a function of applied potential (E) during oxygen evolution in Mn^{2+}-free solutions of 0.10 M P_i buffer in acidic (pH 2.5) and neutral (pH 7.0) conditions. All solutions also contained 1.5–1.9 M KNO_3 supporting electrolyte (an innocent ion at high anodic potentials required to drive OER) to reach a total ionic strength (μ) of 2.0 M. During data collection, solutions were stirred at ~600 rpm with a teflon stir bar (sufficient to remove mass transport limitations as shown previously[34]), and a series of discrete monotonically decreasing potentials were applied to the electrode for 30 s each to allow the current to reach a steady-state value. The highest potential (first point in the series) was held for 200 s to further minimize any pseudocapacitance. All potentials were automatically *iR* compensated for solution and FTO resistance (~17 Ω). Catalyst films were thin (<50 nm) and any resistivity through the film was negligible and not included in *iR* corrections: electrochemical impedance spectroscopy measurements (*vide infra*) estimate ~0.4 Ω. The current–potential data was plotted in the form of log j vs. E (or η) to construct Tafel plots, which were reproducible with independently prepared MnOx samples. Control studies with bare FTO demonstrates that FTO is poor at oxygen evolution and serves as a good substrate since it exhibits high Tafel slopes and current densities for OER of at least an order of magnitude lower than that of MnOx catalyst films.

Faradaic efficiency of oxygen evolution. To determine the percentage of charge passed that contributes to oxygen evolution on MnOx films, a fluorescence-based O_2 sensor (FOXY OR125-GT/AF-MG, Ocean Optics) was used to measure oxygen concentration during sustained electrolysis by chronoamperometry. A custom-built, gas-tight electrochemical H-cell was fit with the O_2 sensor (in a 14/20 port) in the working compartment, and the MnOx catalyst (1 cm^2 film deposited on FTO) and Ag/AgCl reference electrode were connected with glass-sealed electrical leads. The auxiliary compartment contained a Pt mesh electrode. Prior to all measurements, the cell was purged for 1 h with high-purity Ar gas, and a two-point calibration curve (air, 20.9% O_2 and Ar, 0% O_2) was constructed. Activated MnOx catalyst films prepared by multipotential deposition (described earlier) were operated at 0.1 mA/cm^2 in 0.10 M P_i with 1.75 M KNO_3 electrolyte solution at pH 2.5 and 7.0. The excitation and emission phase shift of the O_2 sensor dye were recorded at 2 s intervals and converted to an excited state lifetime (τ). These lifetimes were used to calculate the partial pressure of oxygen (p_{O2}) using a modified Stern-Volmer relation:[60]

$$\tau_0/\tau = 1 + K \times p_{O_2} \quad (1)$$

where K is the Stern-Volmer coefficient, determined by calibration, and τ_0 is the lifetime for 0% O_2. No correction of the partial pressures by Henry's law was required since the amount of dissolved O_2 was small compared to the amount of O_2 in the headspace. These pressures were converted to moles of O_2 by using the ideal gas law and headspace volume of the cell. Finally, the amount of detected O_2 was compared to the theoretical yield of O_2, calculated by dividing the charge passed by 4F.

Electrochemical impedance spectroscopy (EIS). Impedance measurements were conducted on a Gamry Interface 1000 potentiostat for 1 cm^2 FTO as a blank substrate as well as with constant potential deposited MnOx and activated MnOx in 0.10 M P_i buffer, 1.73 M KNO_3 at pH 2.5. Films were evaluated in the region of OER catalysis at 1.65 V with an initial conditioning for 60 s followed by the addition of 5 mV (rms) AC signals from 100 kHz to 0.1 Hz. No *iR* compensation was applied during these measurements. Collected data were analyzed by Gamry Echem Analyst (version 6.30) software to obtain Bode and Nyquist plots and to perform Kramers-Kronig analysis for data quality. Fits were calculated based on a Randles equivalent circuit model employing constant phase and Warburg elements.

Inductively coupled plasma mass spectrometry (ICP-MS). Trace elemental analysis was performed with a quadrupole ICP-MS (Thermo Electron, X-Series ICP-MS with CCT). Because MnOx is resistant to passive dissolution in acid, as-deposited films were digested by voltage cycling (between 1.3 and –0.4 V) in 12 mL of 2% v/v nitric acid (TraceSELECT, Fluka). Manganese and iron calibration standards were prepared from corresponding ICP standard solutions (TraceCERT, Fluka) which enabled the construction of a calibration curve to convert the detected counts for ^{55}Mn and ^{57}Fe to concentrations (in ppm).

Stability during oxygen evolution. The ability of activated MnOx to sustain stable activity for oxygen evolution was assessed by chronoamperometry. Activated MnOx films prepared by multipotential deposition (described earlier) were operated at 0.1 mA/cm^2 in: 100 mM P_i buffer at pH 2.5 and 7.0 with 1.73 M KNO_3 supporting electrolyte and also 0.5 M H_2SO_4 at pH 0.3. Constant potential deposited MnOx, blank FTO, and electrodeposited IrOx (following literature procedures[61]) were also evaluated for comparison. A pre-electrolysis time of 200 s was applied to minimize any pseudocapacitance and solutions were stirred at ~600 rpm throughout the experiment. The potential was recorded over 8 h of contin-

uous catalysis, and stability was evaluated by tracking the change in potential over time. The presence of peroxides in the final solution was tested immediately after the end of catalysis using Quantofix Peroxide 25 test strips (lower limit of detection of <0.5 ppm). In addition, chronoamperometry at higher current densities of 1 mA/cm^2 (geometric area) at pH 2.5 was conducted for activated and constant potential MnOx catalysts electrodeposited on a carbon cloth substrate (AvCarb 1071 HCB), which has ~13 times the surface area of FTO as estimated by electrochemical surface area measurements (following literature procedures[41]).

Tracking electrode mass with a quartz crystal microbalance (QCM). The change in mass on the electrode was recorded in situ using an electrochemical QCM (Gamry eQCM 10M). A 10 MHz platinum-coated quartz crystal (International Crystal Manufacturing Co, Inc.), connected to both the QCM resonator and potentiostat, served as the working electrode, which was placed at the bottom of a static PTFE cell with a Ag/AgCl reference and Pt wire auxiliary electrode. Prior to all experiments, the resonator was locked to the resonant frequency of the crystal and permitted to stabilize for 15 min. The series and parallel resonant frequencies were sampled every second during the experiments and responded similarly (i.e., $\Delta f_s = \Delta f_p$). The change in resonant frequency (Δf) over time was correlated to a change in mass (Δm) on the electrode using the Saurbrey equation:[62]

$$\Delta f = -\frac{2f_0^2}{A\sqrt{\rho_q \mu_q}}\Delta m \qquad (2)$$

where f_0 is the resonant frequency of the crystal, A is the piezoelectrically active crystal area, ρ_0 is the density of quartz, and μ_0 is the shear modulus for the AT-cut quartz. None of the mass changes observed corresponded to a change of greater than 2% of f_0, which validated the use of the Saurbrey equation for analysis. After each experiment, any deposited MnOx film was removed from the Pt-coated quartz crystal by cycling the electrode between 1.7 and –0.1 V in 0.5 M H_2SO_4 (99.99% trace metals basis, Aldrich). Control experiments with only the Pt substrate in Mn^{2+}-free solution were performed for comparison.

Electron microscopy. Morphological changes in MnOx films as a result of deposition protocol were observed by field emission scanning electron microscopy (SEM, Zeiss Supra 55VP). Samples were prepared with high catalyst loadings (32 mC/cm^2 for constant potential MnOx and 2000 cycles for multipotential deposited MnOx) on FTO. The FESEM was operated at a beam voltage of 15.0 kV, working distance of ~8.5 mm, a 30 μm aperture, and an InLens detector.

The crystallinity of MnOx before and after activation was probed by high-resolution transmission electron microscopy (TEM) on a JEOL JEM-2100 equipped with a Gatan CCD. Samples were electrodeposited on a 400-mesh pure carbon film supported on an Au TEM grid (Electron Microscopy Sciences). The grid was partially immersed in the deposition solution and directly employed as the working electrode. Constant potential MnOx was prepared with a short 5 s pulse and multipotential deposited MnOx utilized five complete cycles. Samples were immersed in type I water to remove any residual electrolyte, dried, and then imaged at a beam accelerating voltage of 200 keV using a 250 μm condenser aperture. Images were processed with Gatan DigitalMicrograph software. For constant potential deposited MnOx, crystal planes were identified by computing the FFT of the lattice fringes, masking to each maximum Fourier component, and taking the inverse FFT to isolate an interplanar spacing that was directly measured.

X-ray photoelectron spectroscopy (XPS). The oxidation state of manganese in MnOx samples were examined by XPS using a Thermo Scientific K-Alpha XPS system. MnOx catalyst films were electrodeposited on FTO as described above, and a series of high-purity manganese oxide control compounds were purchased to serve as calibration and comparison markers: $Mn^{II}O$ (99.99% manganosite, Sigma-Aldrich), α-$Mn^{II,III}_3O_4$ (97% hausmannite, Sigma-Aldrich), α-$Mn^{III}_2O_3$ (99.99% bixbyite, Sigma-Aldrich), and β-$Mn^{IV}O_2$ (99.995% pyrolusite, Strem). The phase of these control compounds were verified with powder X-ray diffraction. All samples were illuminated with a 400 μm spot size, monochromated Al Kα X-ray source (1486.6 eV energy and 0.85 eV line width).[63] Surface charging was compensated by a low-energy (0 to 14 eV) electron flood gun. The system was pre-calibrated with Au, Ag, and Cu standards built into the sample stage using an automated routine. The MnO sample was sputtered with Ar ions in advance to remove surface oxidation from air.[49] Powders of the control compounds were mounted by drop casting on high-purity Cu foil (99.9%, Strem) or by attaching to double-sided Cu tape. Survey spectra were collected from 0 to 1350 eV with a step size of 1.0 eV, dwell time of 10 ms, average of 5 scans, and a pass energy of 200 eV. High-resolution spectra used an energy step of 0.1 eV, dwell time of 40 ms, average of at least 75 scans, and a pass energy of 40 eV. High-resolution scans were obtained for the Mn 2p, Mn 3s, Mn 3p, C 1s, and Cu 2p (for samples on Cu substrate) regions. Control and MnOx samples were calibrated to the Cu $2p_{3/2}$ (932.6 eV)[64] and C 1s (284.8 eV)[65] peaks, respectively.

Thin-film and powder X-ray diffraction (XRD). The composition and phase of MnOx thin-film and powder samples were interrogated by XRD. Electrodeposited MnOx films on FTO were prepared as described earlier. Thin-film diffraction patterns were obtained using a Bruker D8 Discover diffractometer configured with a Cu Kα X-ray source (λ = 1.5405 Å, generated at 40 kV and 40 mA) through a 1 mm anti-scattering slit, Göbel mirror, and LynxEye detector with an 8 mm steckblende slit. Knife-edge attachments were used to remove low-angle scattering. The MnOx films on FTO were placed on a PMMA specimen holder, rotated at 3°/min, and scanned in Bragg-Brentano mode from 2θ = 10 to 70° in 0.02° increments with 0.5 s/pt scan rate.

Powder MnOx samples were prepared by the same electrodeposition protocols as described earlier but on multiple 20 × 8 cm FTO plates. The thin films were briefly immersed in type I water to remove any residual solution, dried, and then carefully stripped from the FTO. Catalyst films were ground into a fine powder using a mortar and pestle. This process was repeated until sufficient material was obtained for XRD. The powders were loaded in a small cavity in a Si zero-diffraction plate (MTI Corporation) and inserted into a Bruker D2 Phaser powder diffractometer equipped with a Cu Kα X-ray source (generated at 20 kV and 20 mA; passed through a 1 mm slit) and LynxEye detector. A knife-edge attachment was used to reduce scattered signal, and the stage was rotated by 3°/min. Samples were examined in Bragg-Brentano mode from 2θ = 10 to 75° in 0.02° increments with 0.5 s/pt scan rate.

Diffraction data was analyzed by search-match in Bruker's EVA 3.0 software using the JCPDS–ICDD PDF-2 (Release 2012) database. The data were also compared to patterns collected from control manganese oxide samples (same compounds used for XPS with the addition of δ-$Mn^{+3.7}O_2$, birnessite, synthesized by previously described procedures[66]), loaded in the Si zero-diffraction plate with same XRD experimental parameters as for the MnOx powders.

Atomic pair distribution function (PDF) analysis. Synchrotron X-ray total scattering experiments were conducted at beamline X17A in the National Synchrotron Light Source (NSLS) at Brookhaven National Laboratory. MnOx powder samples and control manganese oxides (same as those for XRD) were packed into 0.0360" ID × 0.0400" OD Kapton capillary tubes (Cole Parmer) and measured at 100 K using a flowing nitrogen cryocooler. The rapid acquisition pair distribution function (RaPDF) technique[67] was used with an X-ray energy of 67.42 keV (λ = 0.1839 Å). A large area 2-D Perkin Elmer detector (2084 × 2084 pixels and 200 × 200 μm pixel size) was mounted orthogonal to the beam path. The raw 2D data were azimuthally integrated and converted to 1-D intensity versus 2θ using FIT2D.[68] PDFgetX3[69] was used to correct and normalize the diffraction data before applying the Fourier transform to obtain the PDF, $G(r)$, according to:

$$G(r) = \frac{2}{\pi}\int_{Q_{\min}}^{Q_{\max}} Q[S(Q) - 1]\sin Qr\, dQ \qquad (3)$$

where Q is the magnitude of the momentum transfer on scattering and $S(Q)$ is the properly corrected and normalized powder diffraction intensity measured from Q_{min} to Q_{max}.[70] $G(r)$ is a measure of the probability of finding a pair of atoms separated by a distance of r. Lanthanum hexaboride (LaB_6) or nickel was measured as the standard material to calibrate the sample-to-detector distance and to determine the values of Q_{damp} and Q_{broad} parameters, which are used during modeling to account for the instrument resolu-

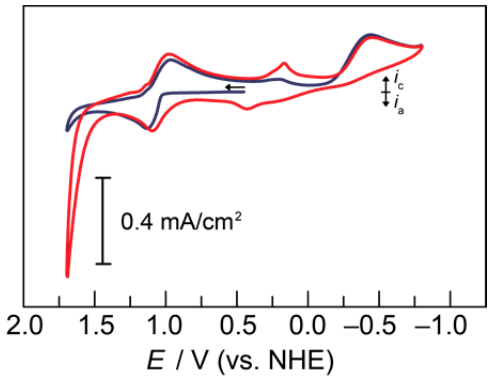

Figure 1. Cyclic voltammogram of a 1 cm^2 FTO electrode in 0.5 mM Mn^{2+} and 0.9 M KNO_3 solution at 100 mV/s scan rate showing the first (blue line ▬) and second (red line ▬) cycles.

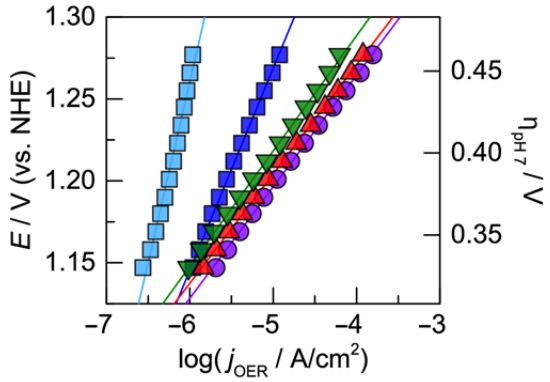

Figure 2. Tafel plots of oxygen evolution in 0.10 M P_i and 1.73 M KNO_3 at pH 7.0 on MnOx films deposited by different deposition protocols: constant potential without buffer (221 mV/decade Tafel slope; light blue, ■), constant potential in MeP_i buffer at pH 8 (123 mV/decade; blue, ■), CV (68 mV/decade; purple, ●), multipotential pulses (67 mV/decade; red, ▲), and cathodization (70 mV/decade; green, ▼).

tion effects on the PDF.[71,72] The sample-to-detector distances for constant potential deposited/cathodized samples and for multipotential deposited sample are 204.264 mm and 204.577 mm, respectively. The refined values were Q_{damp} = 0.0387 $Å^{-1}$ and Q_{broad} = 0.0184 $Å^{-1}$ for constant potential deposited and cathodized samples while Q_{damp} = 0.0409 $Å^{-1}$ and Q_{broad} = 0.0207 $Å^{-1}$ for multipotential deposited sample. They are slightly different since the data were collected on different occasions and the setup was calibrated separately each time. These values were then used as fixed values in subsequent model fits to the PDF data.

PDF modeling was performed with the PDFgui[72] and SrFit[73] programs. Trial PDF fits used birnessite (δ-MnO_2), pyrolusite (β-MnO_2), akhtenkite (ε-MnO_2), hausmannite (α-Mn_3O_4), bixbyite (α-Mn_2O_3), manganosite (MnO), rancieite ($(Ca,Mn^{2+})\ Mn_4^{4+}O_9{\cdot}3H_2O$), and Mn_5O_8 structures. Final fits of the MnOx samples employed structures of birnessite and hausmannite. The birnessite model has the space group C2/m (No. 12), where Mn, O_{OL}, K_{IL}, and O_{IL} atoms are positioned at (0, 0, 0), (x, 0, z), (x, 0, z) and (x, 0, z), respectively, where OL and IL stand for octahedral layer and interlayer, respectively. Water and potassium ion intercalants were introduced between the MnO_6 layers, as reported by Zhu et al.[74] The hausmannite model has the space group $I4_1/amd$ (origin choice 1), with Mn1, Mn2, and O atoms at (0, 0, 0), (1/2, 1/4, 1/8), (0, y, z), respectively. The nanocrystalline nature of MnOx was modeled as the bulk PDF attenuated by a spherical characteristic function,[75–77] which allows us to estimate the crystallite size or the range of structural coherence in the samples.

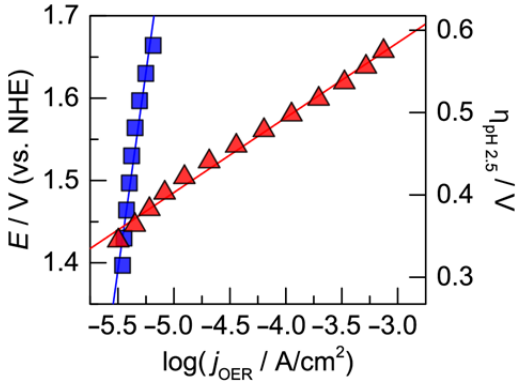

Figure 3. Tafel plots of oxygen evolution in 0.10 M P_i and 1.90 M KNO_3 at pH 2.5 on constant potential deposited MnOx (~650 mV/decade Tafel slope; blue ■) and activated MnOx (91 mV/decade; red ▲).

RESULTS

The oxygen evolution activity of manganese oxide thin films (MnOx) changes as a function of electrodeposition protocol. As has been reported, MnOx films produced by cyclic voltammetry in Mn^{2+} aqueous solutions exhibit higher OER activities compared to films deposited at constant anodic potential.[47] MnOx deposited on the first CV sweep becomes "activated" towards OER on the second cycle (Figure 1). Motivated by this observation, we prepared MnOx films by different electrodeposition protocols and set out to correlate the nature of this activation process with the electrochemistry and structure of the MnOx system.

Electrochemical deposition and Tafel analysis. *Constant potential deposition.* MnOx is typically deposited at constant anodic potential in an aqueous solution containing a Mn^{2+} salt. Following previously described procedures,[33] FTO-coated glass slides were polarized at a constant potential of 0.54 V (vs. NHE unless otherwise stated) in quiescent solutions of Mn^{2+} buffered by MeP_i at pH 8. The resulting brown films were placed in Mn^{2+}-free P_i buffer solutions where the films' OER activity was defined by Tafel analysis. Because there are no methods to accurately normalize current densities to the number of true active sites in the films, Tafel slopes were used as the primary activity descriptor (where lower slope is better) because it is invariant to the number of active sites (*vide infra*). These MnOx films, deposited at constant potential, exhibit ~120 mV/decade Tafel slope at pH 7.0 (Figure 2) and ~650 mV/decade slope at pH 2.5 (Figure 3).[34] MnOx films deposited at constant potential in the absence of a buffer (in just aqueous solutions of Mn^{2+}) yield slightly less active films with Tafel slopes of ~221 mV/decade (Figure 2). Overall, these films display only modest OER activities and are considered "unactivated" in subsequent discussion. For clarity in subsequent discussion, MnOx deposited at constant anodic potential will be denoted "as-deposited".

Cyclic voltammetry deposition. MnOx catalyst films can also be deposited by prolonged cyclic voltammetry (CV). Following previously reported procedures,[47] FTO electrodes were CV cycled in solutions of just aqueous Mn^{2+} (Figure S1a). Films obtained by this method exhibited Tafel slopes of ~74 mV/decade for OER in P_i buffer at pH 7 (Figure S1b). However, CV deposition was difficult

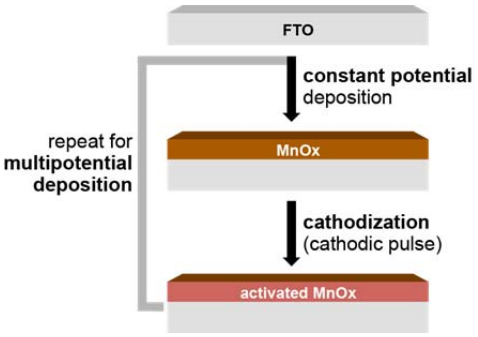

Figure 4. Electrochemical protocols for depositing MnOx on an FTO electrode. Unactivated (as deposited) MnOx (brown) is produced by constant anodic potential deposition. Cathodizing this film by applying a negative potential results in activated MnOx (red). Activation can also occur by CV cycling (not shown) and multipotential deposition (which repeats the anodic–cathodic pulse sequence).

to analyze by electrochemical methods because of high solution resistances (~4 kΩ/cm), which led to broad and shifted CV peaks. Adding KNO_3 supporting electrolyte resulted in sharper CV features (Figure 1) while still retaining the ability to deposit active films that exhibit Tafel slopes of 68 mV/decade for OER at neutral pH (Figure 2). CV-deposited films have lower Tafel slopes than that of as-deposited MnOx films and are considered "activated" for oxygen evolution. In this study, a Tafel slope of approximately 70 mV/decade serves as the benchmark for categorizing catalyst films as "activated".

Multipotential deposition. CV deposition can be deconstructed into a primary anodic event at 1.1 V, where MnOx deposition occurs, followed by a series of reductions at ca. 1.0, 0.1, and –0.6 V (Figure 1). In order to study these redox processes more directly and rigorously, instead of sweeping the potential through these peaks, the potential was held constant at 1.1 V for a short period of time before briefly switching to a lower value, targeting the cathodic peaks near 0.1 and –0.6 V. For clarity, we call this method multipotential deposition. Alternating between anodic and cathodic potentials (see schematic in Figure 4) in a solution of Mn^{2+} and KNO_3 supporting electrolyte resulted in a brown film that grew thicker over cycles. Films produced using a 0.2 V cathodic pulse exhibited a Tafel slope of 92 mV/decade for OER in P_i buffer at pH 7.0. However, a lower slope was observed when a –0.4 V cathodic pulse was employed instead (Figure S2), and the best performing multipotential deposited films were deposited by stepping the electrode between 1.1 V for 3 s and –0.4 V for 2 s. These films displayed a Tafel slope of ~67 mV/decade at neutral pH (Figure 2) and ~91 mV/decade at pH 2.5 (Figure 3), establishing that multipotential deposition produces activated MnOx films.

Cathodization. A further simplification can be applied to multipotential deposition by reducing the procedure to a single cycle: an initial anodic deposition event followed by a final cathodic pulse without any further repetition (see schematic in Figure 4). We call this process "cathodization" in analogy to the more commonly known term "anodization", where an anodic pulse is applied to an existing film (as demonstrated in NiB_i catalyst films[31]). To cathodize MnOx, thin films (3 mC/cm^2 catalyst loading) were first deposited at 1.1 V in a Mn^{2+} solution with KNO_3 supporting electrolyte and then (in the same solution) poised at –0.4 V for 2000 s. These

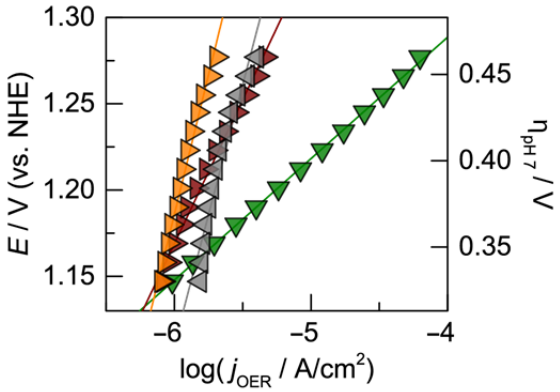

Figure 5. Tafel plots of oxygen evolution in 0.10 M P_i and 1.73 M KNO_3 at pH 7.0 on MnOx films produced by cathodization of MnOx in: Mn^{2+}-less solution (300 mV/decade Tafel slope; grey, ◀), 0.5 mM Mn^{2+} with 100 mM P_i buffer at pH 7.0 (181 mV/decade; brown, ▶), and 0.5 mM Mn^{2+} with 100 mM MeP_i buffer at pH 8.0 (323 mV/decade; orange, ▶). Activated MnOx by cathodization in 0.5 mM Mn^{2+} and 0.9 M KNO_3 solution (70 mV/decade; green, ▼) is provided for comparison.

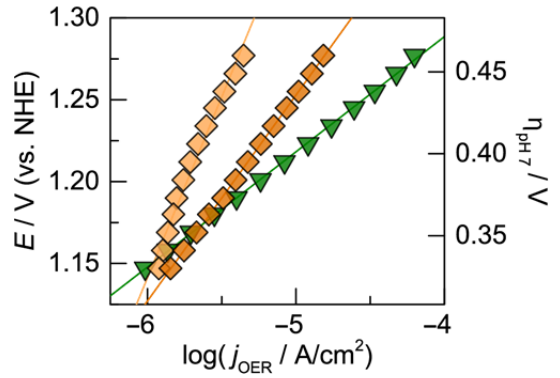

Figure 6. Tafel plots of oxygen evolution in 0.10 M P_i and 1.73 M KNO_3 at pH 7.0 on MnOx films produced by cathodic deposition (221 mV/decade Tafel slope; light orange, ◆) and cathodic deposition followed by short anodic pulse (126 mV/decade; dark orange, ◆). Activated MnOx by cathodization (70 mV/decade; green, ▼) is provided for comparison.

cathodized films were transferred to Mn^{2+}-free P_i buffer, and subsequently evaluated by Tafel analysis for OER activity (Figure 2) demonstrating Tafel slopes of ~70 mV/decade at neutral pH, similar to those of CV and multipotential deposited films. Thus, cathodization in unbuffered Mn^{2+} solutions yields activated MnOx films.

In contrast, when cathodization is performed in Mn^{2+}-free solution or in *buffered* solutions containing Mn^{2+}, no activation was observed. As-deposited MnOx films were subjected to a cathodic potential of –0.4 V in: Mn^{2+}-free solutions containing just KNO_3 supporting electrolyte, Mn^{2+} solutions buffered with P_i at pH 7.0, or Mn^{2+} solutions buffered with MeP_i at pH 8.0. In all cases, steep Tafel slopes of ~200–300 mV/decade were observed for OER at pH 7.0 (Figure 5). These high slopes indicate a regression in OER performance relative to the as-deposited MnOx (with Tafel slope of ~123 mV/decade). These results show that the cathodization

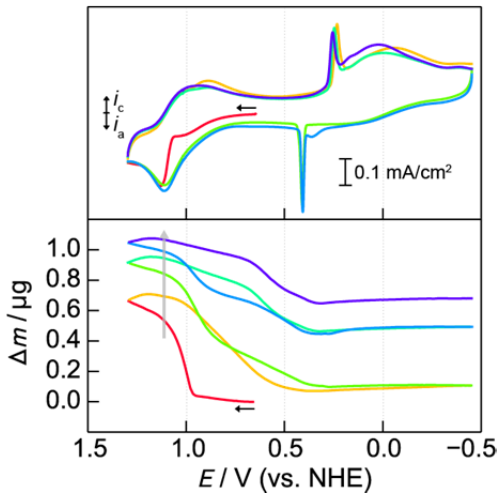

Figure 7. Cyclic voltammogram (*top*) and corresponding change in mass as measured by a quartz crystal microbalance (*bottom*) on a Pt-sputtered quartz electrode in 0.5 mM Mn^{2+} and 0.9 M KNO_3 solution at 50 mV/s scan rate. The scans progress from red to purple lines, and grey arrow indicates increase in mass over time. The current–time view of the same process is shown in Figure S6.

procedure activates MnOx only when performed in Mn^{2+} solutions that are unbuffered.

Cathodic deposition. To check if the initial as-deposited MnOx was necessary for activation, deposition of MnOx films was attempted using only cathodic potentials. FTO electrodes were poised at –0.4 V (the same potential used for cathodization) in a deposition solution containing Mn^{2+} and KNO_3 supporting electrolyte. The FTO remained clear with faint darkening around the edges, which suggested that only a trace amount of catalyst formed. The electrode was evaluated for oxygen evolution in P_i buffer at pH 7, but the resulting Tafel plot (Figure 6) with a slope of ~221 mV/decade demonstrated poor OER performance relative to activated MnOx. When a short anodic pulse was applied to the FTO electrode immediately after cathodic deposition, a thin brown film instantly appeared. The Tafel slope of this film for OER in P_i buffer at neutral pH was ~126 mV/decade, an improvement over purely cathodic deposition but similar to the slope of as-deposited MnOx (~123 mV/decade). However, the Tafel slopes of both cathodically deposited MnOx films were higher than that of activated MnOx (~70 mV/decade), and thus, cathodic deposition does not seem to produce activated MnOx films.

Faradaic efficiency and stability. Evolved oxygen from the catalyst films were measured by a fluorescence O_2 sensor in a gas-tight cell and compared to the amount of charge delivered to the films. The Faradaic efficiency for oxygen evolution was near unity for activated MnOx films operating in neutral and acidic solutions of P_i buffer (Figure S3). In addition, the stability of activated MnOx was evaluated by chronoamperometry at 0.1 mA/cm² over ~8 h of sustained oxygen evolution. In P_i buffer at pH 7.0 and 2.5 and in sulfuric acid at pH 0.3, the films remained both chemically (i.e., no degradation of the film) and electrochemically stable (i.e., no significant change in potential) in both neutral and acidic pH solutions throughout the entirety of the stability test (Figure S4). No peroxides were detected in the final solutions, and Tafel plots of activated MnOx taken before and after the stability tests showed no change in slope

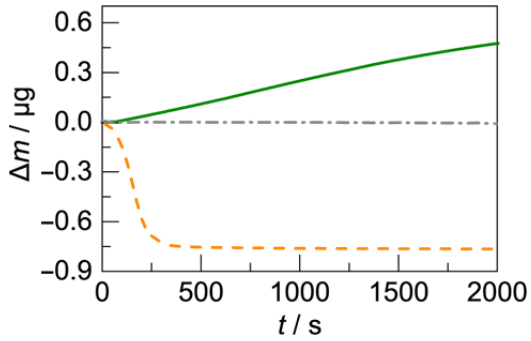

Figure 8. Change in mass as measured by a quartz crystal microbalance on a constant potential deposited MnOx film (of 3 mC/cm² loading, ~0.7 μg) cathodized in: 0.5 mM Mn^{2+} and 0.9 M KNO_3 solution (green, —), Mn^{2+}-free solution of 0.9 M KNO_3 (grey, –•–•), and 0.5 mM Mn^{2+} and 50 mM MeP_i at pH 8 (orange, – – –).

(Figure S5). Overpotentials of ~470 and ~540 mV were required to maintain 0.1 mA/cm² in neutral and acidic (both pH 2.5 and 0.3) solutions, respectively. Consequently to demonstrate higher current densities without increasing applied potential, as-deposited and activated MnOx were electrodeposited on a carbon cloth substrate and operated at 1 mA/cm² (geometric area) in pH 2.5 solution (Figure S4d). The measured electrochemical surface area of the carbon cloth is approximately 14 times greater than the FTO substrates (Figure S6), and this is reflected by the ca. 10-fold increase in current density of activated MnOx (from 0.1 to 1 mA/cm²) at similar overpotential.

Film resistivity and purity. To test if the lower Tafel slope of activated MnOx is the result of decreased electrical resistance of the film when compared to as-deposited MnOx, both systems and a blank FTO electrode were subjected to electrochemical impedance spectroscopy (EIS) during OER at 1.65 V in pH 2.5 solution. The idea behind EIS is that different electrochemical processes can be deconvoluted and isolated at certain frequencies, enabling separation of film properties from catalysis.[78] The resulting Bode and Nyquist plots (Figure S7) were fit to a modified Randles circuit (Figure S7g) which includes: resistive elements for uncompensated (R_u, comprising solution and film resistance) and Faradaic resistance (R_f, incorporating polarization and charge transfer resistance); constant phase elements for solution and film capacitance, Y(α) where α is close to 1, as well as for diffusion limitations using a Warburg element (W_d). Kramers-Kronig analysis indicates high data quality and calculated Bode and Nyquist fits were consistent with experimental data suggesting that this basic Randles circuit was sufficient for describing the electrochemical system—that more complex equivalent circuits were unnecessary. The parameters from the fits (Table S1) show that the uncompensated resistance from FTO and solution resistance totaled ~16.5 Ω and that presence of either as-deposited or activated MnOx only adds ~0.4 Ω of resistance. While the Faradaic resistance decreases from ~18 kΩ to 27 Ω, it should be noted that this value primarily reflects OER kinetics and not film resistance: lower R_f are inversely proportional to higher current densities in Tafel plots.[79] The large decrease in R_f between as-deposited and activated MnOx is consistent with Tafel plots (Figure 3) demonstrating a similar order of magnitude increase in current density. Thus, film resistivity for these thin films plays a negligible role when evaluating their Tafel slopes.

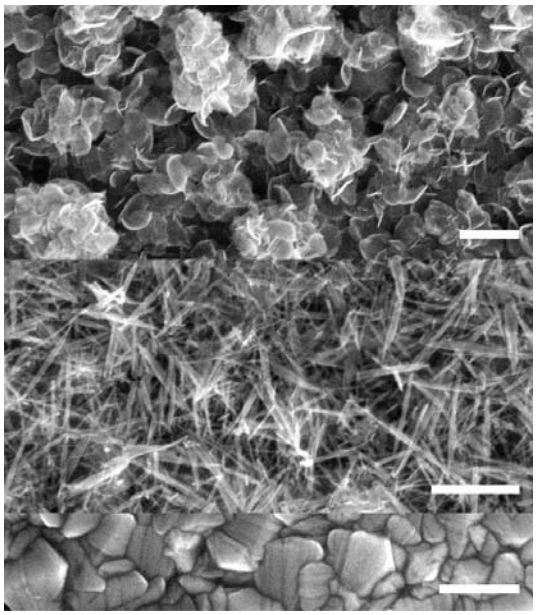

Figure 9. FESEM images of: MnOx deposited at constant potential in MeP_i (*top*) and activated MnOx (*middle*). Both samples were electrodeposited on FTO substrate (*bottom*). Scale bars are 400 nm.

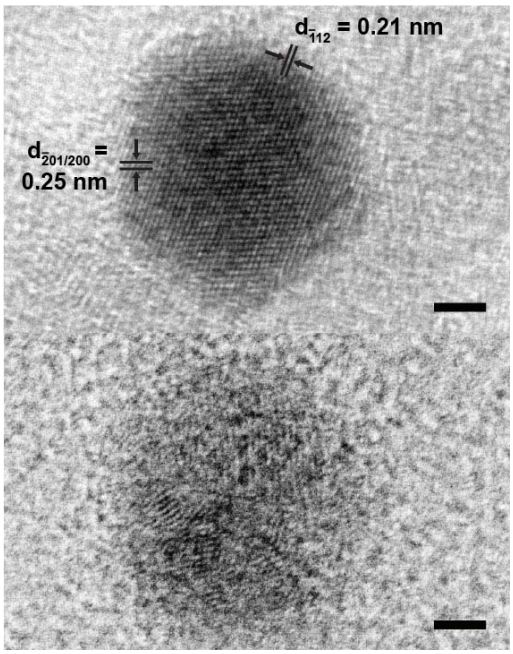

Figure 10. HRTEM images of isolated nanosized domains from MnOx deposited at constant potential (*top*) and from activated MnOx (*bottom*). All samples were electrodeposited on carbon film (visible as amorphous background). Scale bar is 2 nm. Interplanar spacing for constant potential MnOx was measured from the FFT and indexed according to birnessite.

The presence of any trace Fe (in ppm-level concentrations in even high purity reagents) is not responsible for the activation of MnOx films. As-deposited MnOx is not very active for OER, and when these films were anodized in pH 2.5 and 7.0 solutions at high anodic potentials for ~8 h (Figure S4), no increase in OER activity was observed. Similarly, when these films were cathodized in Mn^{2+}-free solutions at neutral pH, subsequent Tafel plots showed that their OER activity diminishes relative to the original films (Figure 5); cathodization in acidic Mn^{2+}-free electrolyte results in slow film dissolution instead of activation. These results are consistent with the negligible amount of Fe in as-deposited MnOx (<10 ppb, corresponding to <0.6% of Mn concentration) as analyzed by inductively coupled plasma mass spectrometry. This is below the ~5% and ~8% Fe threshold where an increase in alkaline OER activity is observed for Ni and Co films, respectively.[80–82] Thus, activation and operation of MnOx films in acidic and neutral pH is not influenced by any trace Fe impurities.

Mass change for electrodeposition protocols. An electrochemical quartz crystal microbalance (QCM) was employed to study the change in mass on a Pt-sputtered quartz electrode for different deposition protocols. For CV (Figures 7 and S8) and multipotential methods (Figure S9) in Mn^{2+} solutions with KNO_3 supporting electrolyte, the electrode mass increased with cycling. Potentials above ~0.9 V facilitated anodic deposition of MnOx. In contrast, a mass decrease was observed on the cathodic sweeps of CVs and on the cathodic pulses of multipotential deposition. However, this rate of decrease drops to zero at more cathodic potentials (below ~0.4 V in Figure 7). Because the total mass loss was always less than the amount of mass deposited, there was net deposition of MnOx over many cycles. For example, three CV cycles resulted in an increase of 1 μg on the electrode. In contrast, CVs taken in a Mn^{2+}-free solution exhibited only 10 ng of mass change, which was attributed to the reversible formation of Pt oxide on the electrode surface (Figure S10). Furthermore, CV deposition in Mn^{2+} solutions buffered with MeP_i at pH 8.0 was unsuccessful with completely reversible mass change and no net mass increase (Figure S11).

For the cathodization process, a thin as-deposited MnOx film on the QCM electrode was poised at –0.4 V in the same solution of Mn^{2+} with KNO_3 supporting electrolyte (Figure 8). As suggested by QCM results from CV and multipotential deposition, there was no mass loss on the electrode at these cathodic potentials. Instead, there was a slight mass increase during cathodization. For comparison, when cathodization was performed in Mn^{2+}-free solutions with KNO_3, no change in mass was observed. Finally, cathodization in Mn^{2+} solutions that are buffered with MeP_i at pH 8.0 led to complete desorption of the pre-deposited MnOx film.

For cathodic deposition, a blank QCM electrode was held at a constant cathodic potential in a solution of Mn^{2+} and KNO_3 supporting electrolyte. There was a faint linear increase in electrode mass of 0.2 μg over 1800 s. However, upon removal of potential, the electrode mass sharply decreased for an overall net zero change in mass (Figure S12a). As described earlier, application of a short anodic pulse immediately following cathodic deposition results in a rapid change in FTO electrode color from clear to brown. The same procedure, applied here with a 30 s anodic pulse on the QCM electrode, led to immediate darkening of the electrode accompanied by a sharp rise in mass, signifying film deposition (Figure S12b). The magnitude of this mass increase of ~0.7 μg over 30 s is approximately 7x greater than the mass increase of ~0.1 μg for 30 s of constant anodic potential deposition of MnOx.

Structural studies. *SEM and TEM.* MnOx films prepared via different deposition routes have distinct morphologies. By SEM, as-deposited MnOx has pedal-like or plate-like features while activated MnOx resembles needles or nanorods (Figure 9). TEM images

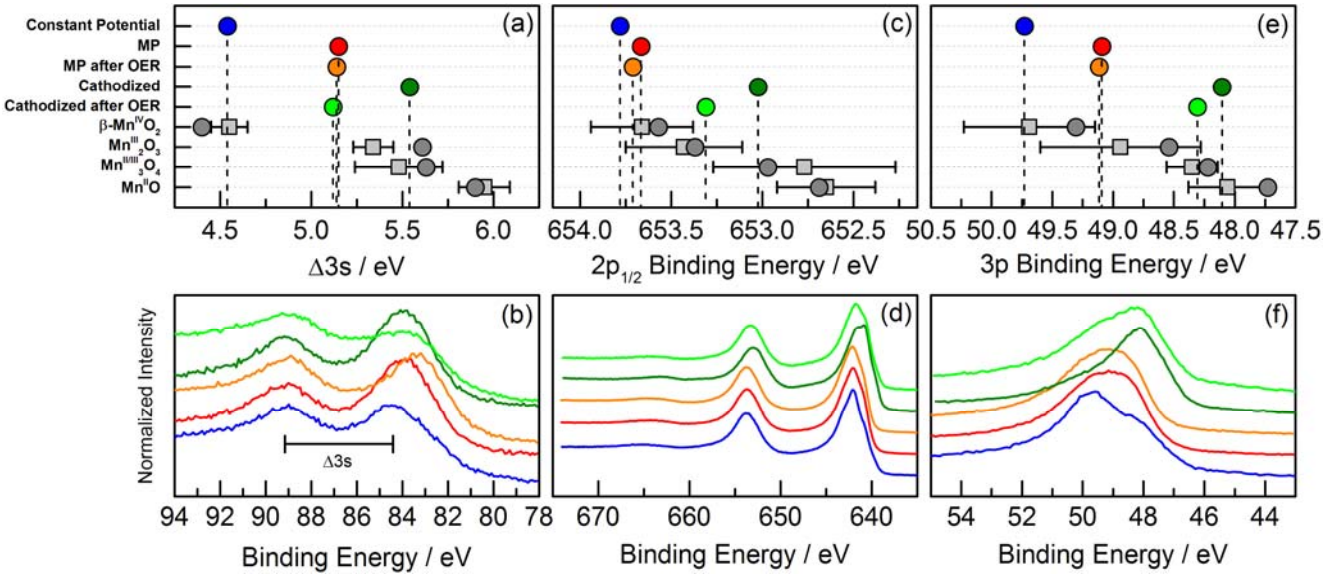

Figure 11. XPS diagnostics for assessing average Mn oxidation state in MnOx films: (a, b) Mn 3s peak splitting width (Δ3s); (c, d) Mn 2p$_{1/2}$ binding energy; (e, f) Mn 3p binding energy. High-resolution spectra are shown in the bottom row for MnOx prepared by: constant potential (blue ●,▬), multipotential (●,▬), multipotential followed by OER (●,▬), cathodization (●,▬), and cathodization followed by OER (●,▬). The top row provides a simplified view of the diagnostic parameters extracted from the spectra with comparison to manganese oxide control compounds (grey, darker ● is from this paper, lighter ■ and black bars is compiled from literature). High-resolution XPS spectra for control compounds are shown in Figure S13.

show differences in crystallinity between as-deposited and activated MnOx films (Figure 10). While both samples are nanocrystalline, as-deposited MnOx exhibits coherent crystalline domains of ~8–10 nm while activated MnOx is considerably disordered: the domain size decreases to ~2–4 nm and edges of the catalyst become amorphous.

X-ray photoelectron spectroscopy. XPS was employed for observing changes in the average manganese oxidation state of MnOx samples by monitoring the binding energy shift, satellite peak splitting, and exchange peak splitting for the Mn 2p, 3s, and 3p peaks. These parameters for a series of control manganese oxides ($Mn^{IV}O_2$, $Mn^{III}_2O_3$, $Mn^{II,III}_3O_4$, and $Mn^{II}O$) are well-documented as diagnostics of the Mn oxidation state,[49,83–92,107] and literature XPS data for manganese oxides have been included in subsequent analysis for comparison.

MnOx samples were prepared with the different electrodeposition protocols on FTO, and manganese oxide control samples were mounted on Cu tape. Survey spectra of all compounds indicated no presence of impurities. High-resolution scans were recorded for the Mn 2p, 3s, and 3p regions (Figure 11 and Figure S13). A reliable diagnostic for Mn oxidation state is the degree of Mn 3s peak splitting that is caused primarily by the exchange interaction between the 3s and 3d electrons.[85,89,93] When applied to control and MnOx samples (Figure 11a and 11b), as-deposited MnOx is MnO_2-like, which was expected from our previous mechanistic study.[33] However, cathodized MnOx is Mn_2O_3 or Mn_3O_4-like, where the larger Mn 3s peak splitting suggests that there is significant Mn^{3+} in the bulk cathodized film.

For multipotential deposited MnOx, the Mn 3s peak splitting is between that of as-deposited and cathodized MnOx (Figure 11a and 11b), which indicates that the average Mn oxidation state has increased slightly and is between +3 and +4. This "mixed" $Mn^{3+/4+}$ oxide retains its formal oxidation state even after operation at high anodic potentials for oxygen evolution, which demonstrates that this new phase is stable and does not simply convert slowly back to the as-deposited MnO_2-like film. Similarly, cathodized MnOx films after OER exhibit a similar oxidation state as multipotential deposited MnOx films, demonstrating that both methods of activation access the same mixed $Mn^{3+/4+}$ state during oxygen evolution.

Other diagnostics include the Mn 2p$_{1/2}$ and 3p binding energies. The 2p$_{1/2}$ peak arises from spin-orbit coupling of the 2p electrons, which splits the 2p orbitals into 2p$_{1/2}$ and 2p$_{3/2}$ energy levels.[85,88,94] Both 2p$_{1/2}$ and 3p binding energies increase with higher Mn oxidation state, as observed in control manganese oxide compounds (Figure 11c to 11f). However, the accuracy of absolute binding energies is affected by surface charging and depends on spectrometer calibration. As a consequence, literature compiled values for the control compounds exhibit wide standard deviations. To increase the accuracy of measured binding energies, the XPS spectrometer was calibrated to Au, Ag, and Cu standards before experiments and binding energies were corrected via the Cu 2p$_{3/2}$ peak for samples on Cu tape or via the C 1s peak for electrodeposited MnOx samples on FTO. Generally, results from binding energy analysis correlate with those from the Mn 3s exchange energy diagnostic: as-deposited MnOx is MnO_2-like, cathodized MnOx contains significant Mn^{3+}, and multipotential deposited as well as cathodized MnOx films after water oxidation have an average oxidation state between +3 and +4. We note, multipotential deposited MnOx retained the same oxidation state before and after OER.

Powder X-ray diffraction (XRD). Composition and phase identification by XRD were initially applied to thin films of MnOx electrodeposited by different protocols on FTO. In the conventional Bragg-Brentano configuration, however, the observed diffraction patterns were all matched to the underlying FTO substrate (Figure

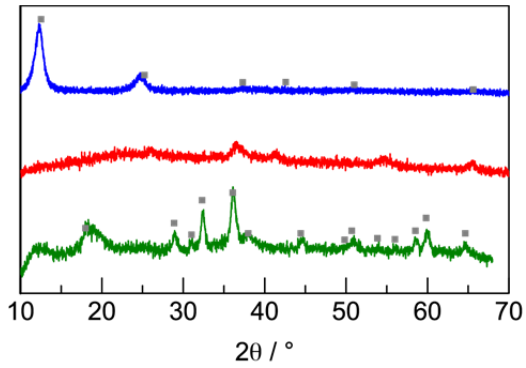

Figure 12. Powder X-ray diffraction patterns of MnOx prepared by: constant potential (top —), cathodization (bottom —), and multipotential (middle —) deposition. Constant potential MnOx (blue —) matches birnessite (grey ■, JCPDS #01-087-1497) while cathodized samples (green —) matches hausmannite (grey ■, JCPDS #24-0734). Multipotential MnOx (red —) was highly disordered and the phase was undetermined by XRD.

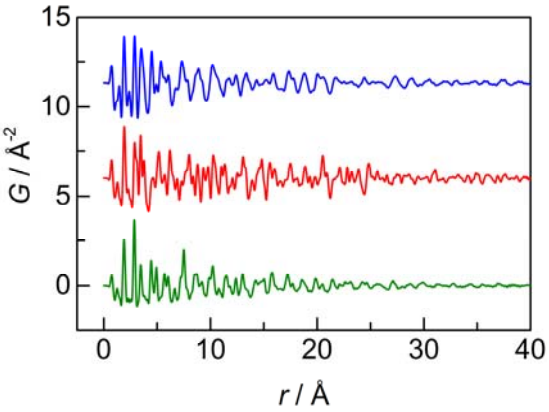

Figure 13. Atomic pair distribution functions (PDFs) of MnOx prepared by different deposition protocols: constant potential (top —), multipotential (middle —), and cathodization (bottom —). PDFs are truncated at 40 Å. PDFs for manganese oxide control samples are in Figure S16.

S14). The as-deposited MnOx thin film produced a weak and broad peak at ca. 2θ = 12°, but there were no additional non-FTO features to facilitate a structural search.

To eliminate the intense FTO diffraction peaks, MnOx catalyst films were examined as powders: electrodeposited variants of MnOx films were mechanically separated from the FTO and ground into fine particles. XRD was performed on these samples (Figure 12) as well as a series of manganese oxide control compounds for comparative purposes (Figure S15). All control compounds displayed well-defined diffraction patterns that were phase matched to JCPDS–ICDD entries.

For MnOx samples, as-deposited MnOx exhibited strong diffraction peaks at ca. 2θ = 12 and 25° that were characteristic of birnessite (δ-MnO_2). The diffraction pattern for cathodized MnOx matched hausmannite (α-Mn_3O_4) with three prominent characteristic peaks at ca. 2θ = 29, 32, and 37°. In contrast, multipotential deposited MnOx samples exhibited very faint and broad peaks that appeared atop an intense background. The poor crystallinity of multipotential deposited MnOx was insufficient for reliable phase matching using an in-house X-ray source and conventional XRD.

X-ray pair distribution function (PDF). To obtain structural information on low crystallinity MnOx films (in particular, multipotential deposited MnOx), total X-ray scattering (both Bragg and diffuse) from sample powders over a wide range of momentum transfer (Q) was collected using a synchrotron X-ray source. Data were collected to short d-spacings of a few tenths of an angstrom and then Fourier transformed to obtain the probability density of atomic pairs as a function of atomic distance (i.e., the pair distribution function).[70,95,96] Structural analysis was performed by developing a model of the catalyst and then optimizing the model's computed PDF to fit the experimental PDF.[70,95,96]

The domain size or crystallinity of MnOx catalysts was estimated by examining the decay of the PDF plots for control manganese oxides (Figures S16) and MnOx samples prepared by different electrodeposition protocols (Figure 13). The PDF peaks for the control compounds extend beyond the plot cutoff of 40 Å, indicating that the control samples are highly crystalline as anticipated from their sharp XRD patterns (Figure S15). In contrast, the PDF peaks in electrodeposited MnOx samples disappear at lower r values, indicating a smaller structural coherence. Spherical PDF models of multipotential deposited and cathodized MnOx suggest a domain size of ~30–50 Å for these samples, which is consistent with estimations by TEM.

The similarity of MnOx samples to control compounds was surveyed by calculating the Pearson's product–moment correlation coefficient R over discrete ranges of atomic distances (Table S2). This parameter indicates the similarity between two PDF datasets and is calculated by:

$$R = \frac{1}{n-1}\sum_{i=1}^{n}\left(\frac{X_i - \bar{X}}{\sigma_x}\right)\left(\frac{Y_i - \bar{Y}}{\sigma_y}\right) \quad (4)$$

where $\bar{X}$, σ_x, and $\bar{Y}$, σ_y are the mean value and standard deviation for the first and second datasets respectively.[97,98] The Pearson's coefficient has the value between –1 and 1 where the two bounds indicate complete anti-correlation and correlation, respectively. Consistent with XRD results, as-deposited MnOx exhibits strong similarity to birnessite (R = 0.81–0.92) while cathodized MnOx is best correlated to hausmannite (R = ~0.80). However, cathodized MnOx is also moderately similar to birnessite (R = 0.60–0.76) and suggests the presence of a mixed phase of hausmannite and birnessite, which was undetected by XRD. Multipotential deposited MnOx largely resembles birnessite, although the correlation diminishes in the intermediate range.

The composition and phases suggested by Pearson's coefficient analysis were employed in structural modeling of the PDF data. Initially, the birnessite structure was adopted for as-deposited and multipotential deposited MnOx; and the hausmannite structure for cathodized MnOx. The PDF fits (Figure 14 with fit results summarized in Table S3) were performed in an r range up to 40 Å that covers local to intermediate structure, and the nanoparticulate nature of the samples was accounted for by a spherical envelope function.

For as-deposited MnOx, the best fit was achieved with the birnessite model whereas the PDF of cathodized MnOx required a

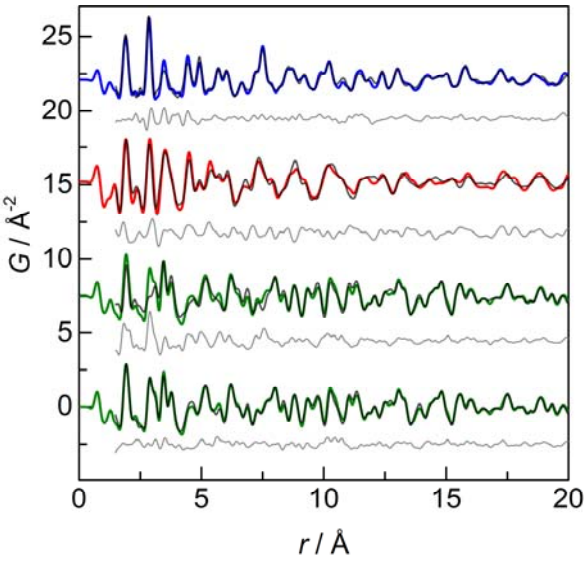

Figure 14. Calculated PDF model fits (black) overlaid on experimental PDF traces of MnOx catalysts prepared by different deposition methods: constant potential (blue —), multipotential (red —), and cathodization (green —). The cathodized sample was fit in two ways: hausmannite structure alone (top green —) and a two-phase birnessite and hausmannite fit (bottom green —). The difference curves (grey —) between the calculated and experimental PDFs are offset below each sample.

two-phase fit of both birnessite and hausmannite (Figure 14). The initial guess for cathodized MnOx consisted of a single hausmannite phase where features in the *r* range above 10 Å were well-matched according to the difference curve between the experimental and calculated PDF. However, there remained significant unfit signal in the low *r* range below 10 Å. According to the Pearson coefficients for cathodized MnOx, the experimental PDF in this short *r* range had a secondary correlation to birnessite, and thus, a two-phase fit was introduced using both hausmannite and birnessite structures. The thermal factors, atomic positions, and occupancies were inherited from previous fits and only scale factors, lattice parameters, and diameters (i.e., particle sizes) for both phases were tuned. The two-phase model improved the PDF fit for cathodized MnOx and successfully captured previously unfit structural features in the low *r* range. Structural coherence for the birnessite component exists at short *r* range while the hausmannite component is correlated over longer intermediate *r* range. The mole fraction of birnessite refined from the fit is ~68%, indicating that the majority of the sample is actually birnessite.

Trial fits of the multipotential deposited MnOx sample were performed against birnessite (δ-MnO_2), pyrolusite (β-MnO_2), akhtenkite (ε-MnO_2), hausmannite (α-Mn_3O_4), bixbyite (α-Mn_2O_3), manganosite (MnO), rancieite ((Ca,Mn^{2+}) $Mn_4^{4+}O_9 \cdot 3H_2O$), and Mn_5O_8 structures. The birnessite model had the best goodness-of-fit factor with low residuals in the short *r* range but displayed deviations between the experimental and calculated PDF in the intermediate *r* range (Figure 14). To account for the unfit signal at higher *r*, a two-phase fit was introduced with birnessite as the first component and the following candidates as the second phase: bixbyite (α-Mn_2O_3), hausmannite (α-Mn_3O_4), akhtenkite (ε-MnO_2), rancieite ((Ca,Mn^{2+})$Mn_4^{4+}O_9 \cdot 3H_2O$), and Mn_5O_8. Both least squares and differential evolution algorithms were employed to optimize the two-phase fits. However, no improvement to the fit was obtained compared to a single-phase birnessite model. In addition, changing the shape function of the model from a spherical to a cylindrical envelope results in only a ~1% improvement to the fit. The poor fit at high *r* range is not due to the model lacking inclusion of additional phases or an incorrect shape function but likely an inherent structural phenomenon of multipotential deposited MnOx.

DISCUSSION

The acid stability of electrodeposited manganese oxide (denoted MnOx) prepared at constant potential is derived from the interplay of deposition[33] and oxygen evolution[34] mechanisms. However, as-deposited MnOx catalysts, though stable in acid, exhibit only modest OER activity at neutral pH (~120 mV/decade Tafel slope) and low activity (~650 mV/decade) in acidic conditions.[34] Methods to increase catalyst activity include surface modification (e.g., binding polyallylamines to surface Mn sites[99]) or mixing other metals in the films (e.g. Mn/Fe,[100] Mn/Co,[101] Mn/Co/Fe,[102,103] Mn/Fe/Cr,[100,104] La/Mn,[105,106] La/Sr/Mn,[105,106] etc.). We show here that MnOx activity may be increased by an electrochemically-induced phase change. By varying the voltage during electrodeposition, it is possible to access thermodynamically stable manganese oxide phases, as suggested by the Pourbaix diagram of manganese,[25] or trap the film in kinetically stable oxide phases. Polymorphs of chemically-prepared manganese oxides containing lower valent Mn ions (such as Mn^{3+} and Mn^{2+}) exhibit greater OER activity than that of MnO_2 oxides,[48] which is the phase produced by constant anodic potential electrodeposition.[34,47,49,107] Similarly, manganese oxide films deposited by cyclic voltammetry[47,49] are more active for OER than those deposited at constant potential. X-ray absorption studies (XANES and EXAFS) on these CV deposited films demonstrate an average Mn oxidation state of +3.6 to +3.8, respectively, instead of the expected +4.0 of $Mn^{IV}O_2$ (i.e., pyrolusite).[47,49] In addition, powder X-ray diffraction on CV deposited film indicates the presence of α-Mn_2O_3.[49] These observations suggest that CV deposition may be a method for accessing different phases of manganese oxides. With this backdrop in mind, we explored other techniques for creating active electrodeposited manganese oxides and simplified the processes down to the essential steps required for activation. Spectroscopic and structural analysis then guided our mechanistic proposal for the activation process.

Electrochemical activation of MnOx. Tafel slopes for the OER differentiate between "non-activated" and "activated" MnOx films. Tafel slopes, as opposed to current densities, offers a more reliable method to compare catalyst films prepared by different electrodeposition protocols because it is difficult to correctly normalize current by the number of active sites in the electrodeposited material.[108] For example, the rate and amount of catalyst deposited vary between methods of preparation. Unlike in constant potential electrodeposition where the charge passed could be directly correlated with catalyst loading, these deposition protocols alternate between anodic and cathodic currents, and thus the total charge passed is in constant flux. By using a QCM, the deposition protocols were adjusted such that catalyst films had similar mass loadings. However even then, the number of active sites in films of the same mass may differ because of changes in film structure or exposed surface area.

Obtaining accurate surface area measurements of thin films is challenging, but the more fundamental issue is that the number of true active sites in a catalyst may be a fraction of its accessible surface area. For example, there are different catalyst regions: planes, edges, grain boundaries, and amorphous domains. Each region may have different manganese oxidation states and oxidic environments with one region containing the dominant "active sites", and it is still an open problem in the field to accurately quantify the number of active sites in catalyst films.

For a Tafel plot, increasing the number of active sites will raise the exchange current density (i.e., the *y*-intercept), which leads to shifting of the plot to higher activities. However, the Tafel slope will still remain the same, because it is only affected by the kinetics of the reaction (assuming that the data was collected in conditions of kinetic control), which involves the type of active site and not its quantity.[78] Thus, instead of emphasizing absolute activity in terms of current density normalized by mass or surface area, we compare the performance of MnOx catalysts by their Tafel slopes for OER, which does not depend on the quantity of active sites in the films.

The representative cases for describing "non-activated" and "activated" MnOx films are constant potential (denoted "as-deposited") and CV deposition, respectively. As-deposited MnOx establishes the baseline case that we sought to improve upon; these films are deposited in MeP_i buffer at pH 8.0 and exhibits a ~123 mV/decade slope at neutral pH (Figure 2).[34] They can also be formed in the absence of a buffer, but the resulting films are even less active with higher Tafel slopes. In contrast, CV deposited films are more active for the OER with Tafel slopes of ~68 mV/decade at pH 7.0 (Figure 2 and consistent with values reported in literature).[47,49] For similar mass loading and geometric area, at an overpotential of 450 mV, CV deposited MnOx displays 10 and 100 times greater current density than MnOx deposited at constant potential from MeP_i and without buffer, respectively. Thus, CV deposited films represent the benchmark for "activated" MnOx and serve as a reference point for comparison to other electrodeposition methods.

CV deposition was simplified by removing slow potential sweeping and by focusing instead on short anodic and cathodic pulses at fixed potentials. In the multipotential method, MnOx is deposited by alternating between two potentials continuously (see schematic in Figure 4) and results in an active MnOx film with a Tafel slope of ~67 mV/decade at neutral pH (Figure 2). More fundamentally, a MnOx film can be deposited at an anodic potential and then subjected to a cathodic pulse. This procedure is called cathodization and also produces activated MnOx films with low Tafel slopes of ~70 mV/decade (Figure 2). These results demonstrate that we can take a pre-existing MnOx film (deposited at constant potential) that has modest activity, apply a simple cathodic procedure (e.g., cathodization), and significantly increase the OER activity of the catalyst.

By simplifying CV deposition to cathodization, we observe that the use of a cathodic pulse is crucial for producing activated MnOx films. Cathodic deposition is prevalent for some materials including Mn,[109–112] Co,[113–117] and Ni[118–121] oxide films and even metal organic frameworks[122] deposited at negative potentials. In these cases, supporting electrolyte (such as NO_3^-) is reduced at the electrode surface leading to the generation of hydroxide species.[123] Hydroxide anions react with metal cations to precipitate an oxidic film. However in practice, MnOx does not deposit well at cathodic potentials: the FTO electrode remained transparent when held at negative potentials. QCM studies demonstrate that there is a slight increase in electrode mass during deposition but that this species is poorly adhesive and desorbs back into solution when the electrode is at open circuit (Figure S12a). Tafel plots of these films (before complete mass loss) exhibit poor slopes (~221 mV/decade, Figure 6) that resemble unactivated MnOx deposited at constant anodic potential from non-buffering electrolyte. The lack of significant film formation and the decrease in electrode mass upon removal of applied potential is attributed to poorly adhesive $Mn(OH)_2$ species, generated by the reaction of Mn^{2+} with OH^- produced near the electrode.[25] To stabilize the film, a short anodic pulse was introduced immediately after cathodic deposition to convert the film into a more adhesive manganese oxide. This additional step tested if anodic conditioning of cathodically deposited MnOx resulted in active films and is conceptually similar to multipotential deposition where cathodic pulses are followed by anodic pulses in a repeating cycle. Indeed as observed by QCM, application of a short 30 s anodic pulse to the cathodically deposited film resulted in a sharp mass increase (Figure S12b), and the resulting brown film was resistant to rinsing. However, the Tafel slope of these films was ~126 mV/decade (Figure 6), which is similar to inactive as-deposited MnOx. Therefore, cathodic deposition is not responsible for activation of MnOx films.

Alternatively, we find that a cathodic pulse applied to as-deposited MnOx causes an irreversible phase change. Precedent for this process comes from the Pourbaix diagram[25] of manganese and also in the supercapacitor literature: MnO_2 supercapacitors normally exhibit reversible conversion between MnO_2 and MnOOH during charging and discharging, but if the potential range of cycling is extended cathodically, there is an irreversible compositional change from MnO_2 to a Mn_2O_3, which destroys the capacitor.[124,125] Our studies also point to a cathodically-induced phase change but triggered by a chemical reaction between manganese in solution and on the electrode. Evidence for this process comes from the observation that inactive films (~300 mV/decade, Figure 5) are obtained when as-deposited MnOx films are cathodized in a solution containing just KNO_3 supporting electrolyte. Thus, activation of as-deposited MnOx film does not occur in Mn^{2+}-free solution, suggesting that the presence of Mn^{2+} during the cathodic pulse is a crucial ingredient. Given that activation requires both Mn^{2+} in solution and a pre-existing MnOx film on the electrode, our results are in line with the well-known comproportionation reaction between Mn^{4+} and Mn^{2+} to yield Mn^{3+}:[54,126–128]

$$\delta\text{-}Mn^{IV}O_2 + 2\ Mn^{II}(OH)_2 \rightarrow \alpha\text{-}Mn_3{}^{II,III}O_4 + 2\ H_2O \qquad (5)$$

The presence of δ-MnO_2 (birnessite) as the reactant and α-Mn_3O_4 (hausmannite) as the product is supported by structural studies (vide infra). Birnessite is a layered structure consisting of edge-sharing MnO_6 octahedra with water and K^+ ions intercalated between the layers (Figure 15). The hausmannite structure is of spinel type that contains corner-sharing MnO_4 tetrahedrons and edge-sharing MnO_6 octahedra where Mn^{2+} and Mn^{3+} ions reside in the former and the latter, respectively (Figure 15). The contention that hausmannite is a more active phase of manganese oxide for OER is consistent with previous proposals that hausmannite and bixbyite

(both containing significant fraction of Mn^{3+}) are the most active polymorphs of manganese oxides.[48] Indeed, we find that our activated MnOx films contain greater Mn^{3+} valency than that of as-deposited MnOx films (Figure 11). For our case, hausmannite is the predominant material as neither XRD nor PDF could determine the presence of α-Mn_2O_3 (bixbyite) in cathodized films (vide infra).

The Mn^{4+}/Mn^{2+} comproportionation reaction is accelerated in the presence of base and is consistent with the local alkaline pH gradient formed by the generation of OH^- during the reduction of nitrate. Indeed, when the mass of the electrode is monitored during the cathodization activation process, the mass increases during the cathodic pulse, signifying the deposition of additional material (Figure 8). In contrast, when cathodization of a pre-existing MnOx film is performed in Mn^{2+}-free solution, no mass change is observed and the resulting film is not active (Figure 8). In addition, suppression of OH^- generation in well-buffered Mn^{2+} solutions such as MeP_i at pH 8 causes complete film loss (Figure 8) as the MnOx film in the absence of base can be fully reduced to soluble Mn^{2+}. As expected, films cathodized in MeP_i buffer display no increase in OER activity, as demonstrated by its high Tafel slopes for OER (~323 mV/decade, Figure 5). Although Wiechen et. al. observe a dependence of the cation type in birnessite on OER activity,[129] the identity of the supporting electrolyte cation during deposition does not seem to affect activation in this study since CV deposition in Mn^{2+} solution without any supporting electrolyte still results in active films (Figure S1) as long as OH^- is generated (i.e. in this case, through hydrogen evolution). These control experiments establish that a crucial step in activation is a phase change triggered by the comproportionation of a pre-existing constant anodic potential deposited MnOx film with cathodically generated solution-phase $Mn(OH)_2$.

Nature of activated MnOx. The phase change of MnOx during activation is qualitatively suggested by SEM, where MnOx films prepared via different deposition routes had different morphologies (Figure 9): as-deposited MnOx features plates or pedals while activated MnOx resembles needles or nanorods. Similar morphologies have been observed for different manganese oxide compositions and polymorphs.[52,130–133] XPS was used to monitor the change in average Mn oxidation state in the films as a function of deposition method. Because XPS is a surface-confined technique, it is well suited for studying thin films. Using the Mn 3s peak splitting distance as the primary diagnostic for comparing electrodeposited films to control compounds, results from XPS were consistent with a birnessite-like phase for as-deposited MnOx and a hausmannite-like phase for cathodized MnOx (Figure 11), which support the comproportionation mechanism shown in Eq. 5. Notwithstanding, the limitations of using XPS for manganese oxide films has been emphasized;[49,107] the diagnostics for Mn_2O_3 and Mn_3O_4 are too similar to resolve with XPS. In addition, although it is possible to extract information about the chemical environment by XPS and thus further probe the phase of the film, in practice, the limitations of in-house X-ray sources lead to broad peaks; obtaining structural information required extensive peak fitting, which is complex for the Mn $2p_{3/2}$ peak.[92,88]

Direct structural information was obtained from X-ray diffraction. Diffraction off of MnOx thin films revealed only substrate peaks, suggesting that the catalyst films were poorly crystalline.

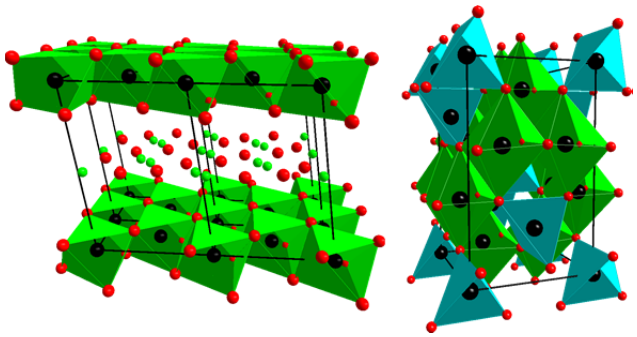

Figure 15. Polyhedral structural models for birnessite (δ-MnO_2, *left*) and hausmannite (α-Mn_3O_4, *right*) where Mn, O, and K atoms are in black, red, and green, respectively. In hausmannite, green and blue regions represent the MnO_6 octahedron and MnO_4 tetrahedron, respectively.

Indeed, TEM images show domain sizes of ~8–10 nm for as-deposited MnOx and ~2–4 nm for activated MnOx (Figure 10). This nanocrystalline nature of MnOx significantly broadens any diffraction peak,[134] and given the low intensity of these peaks, the diffraction patterns were buried in the FTO substrate background (Figure S14). Weak signal intensity was exacerbated by the use of conventional Bragg-Brentano XRD, which is not well suited for thin-films because the μm penetration depth of X-rays in this configuration largely samples the underlying substrate and not the thin film. Moreover, thin films comprise a small amount of catalyst material over a wide area, which further reduces signal intensity. Grazing incidence XRD (recently employed for our CoP_i films on FTO[135]) and in-plane XRD can overcome these challenges;[136] however, for the studies reported herein, we found that the most direct solution was to separate catalyst films from the FTO and prepare the material as a powder for study with conventional Bragg-Brentano diffraction. XRD patterns of these catalyst powders obtained from as-deposited and cathodized MnOx match birnessite and hausmannite, respectively (Figure 12). These results are further support MnOx activation by the comproportionation chemistry of Eq. 5.

Whereas the hausmannite phase is produced upon activation of MnOx films by Eq. 5, it is not preserved during OER. XPS spectra comparing the Mn 3s peak splitting in cathodized MnOx before and after OER demonstrates that the average oxidation state of Mn in these films increases with application of the higher anodic potentials required for oxygen evolution (Figure 11). The final state of cathodized films after OER is similar to that of multipotential deposited films. This result suggests that these films have converged to a similar active phase. Indeed, multipotential deposited MnOx may be viewed as cathodized films that have been subjected to additional anodic pulses (see schematic in Figure 4). This explains why both cathodized and multipotential deposited MnOx have similar Tafel slopes for OER (Figure 2).

To delve more deeply into defining the structure–activity relationship of these films, we employed pair distribution function (PDF) analysis of X-ray diffraction data, which describes the probability density of finding an atomic pair separated by a given distance. We and others have found PDF to be a powerful technique for studying electrodeposited materials that are amorphous.[137,138] Whereas XRD only uses the Bragg diffraction signal, PDF records

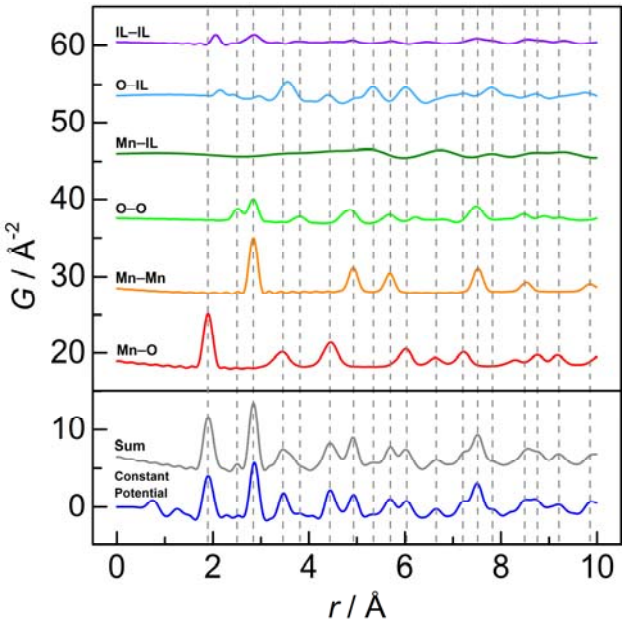

Figure 16. Decomposition of the PDF of the calculated birnessite fit (bottom grey ▬) into contributions from primary atomic pairs where IL denotes interlayer species including K and O (from H_2O) atoms (see Figure 15a for 3D model). The intensity of the top four curves (IL–IL, O–IL, Mn–IL, and O–O) have been magnified 2x for clarity. The experimental PDF for constant potential deposited MnOx is provided for comparison (bottom blue).

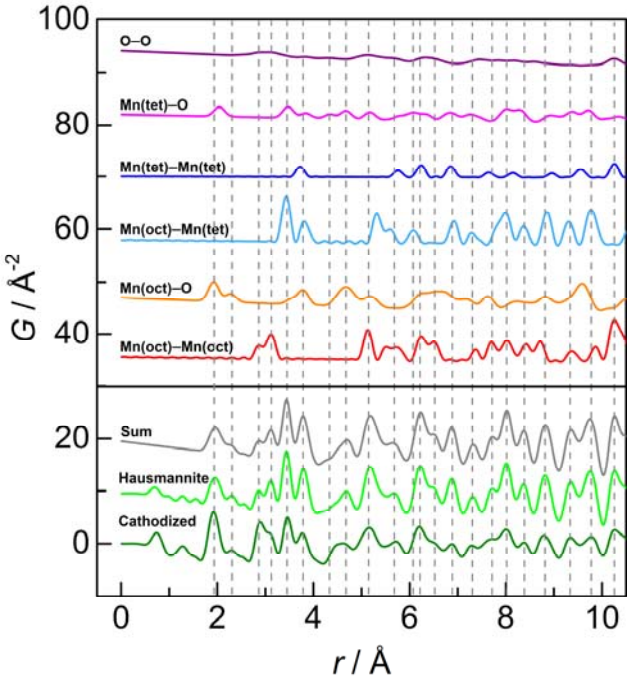

Figure 17. Decomposition of the PDF of the calculated hausmannite fit (bottom grey ▬) into contributions from primary atomic pairs where Mn(oct) and Mn(tet) refer to a Mn atom in octahedral and tetrahedral geometry, respectively (see Figure 15b for 3D model). The experimental PDFs for α-Mn_3O_4 (hausmannite, bottom light green ▬) and cathodized MnOx (bottom dark green ▬) are provided for comparison.

the total X-ray scattering (both Bragg and diffuse). The technique is superior for multipotential deposited MnOx, because the material exhibits poor Bragg diffraction but strong diffuse scattering (which manifests as a broad background signal) in XRD diffraction patterns. Thus, PDF can elucidate the structure of disordered materials in cases where XRD cannot. First, the PDFs of as-deposited and cathodized MnOx were compared to the structural models determined by XRD. As expected for as-deposited MnOx, the birnessite model provides a good fit to PDF data, capturing all of the main structural features of the sample as demonstrated by deconstructing its PDF into component atomic pairs (Figure 16). Similarly, the initial fit of cathodized MnOx to a hausmannite model reproduced the primary structural components in the PDF (Figure 17), particularly in the intermediate *r* range above ~10 Å. However, the single phase fit was insufficient for fully describing the local *r* range (below ~10 Å) and required adding a secondary phase of birnessite in the model (Figure 14). The final fit comprising birnessite in the short range and hausmannite in the intermediate range suggest that the cathodization procedure only converts the outer layers of unactivated MnOx domains (which have the birnessite phase) to hausmannite. This is consistent with the proposed mechanism of Eq. 5 where activation of MnOx involves a phase conversion induced by the comproportionation of birnessite with $Mn(OH)_2$, generated in solution, to produce hausmannite. This reaction occurs at the catalyst–solution interface, which is self-limiting and prevents full transformation of the catalyst domains to hausmannite.

Whereas XRD could not resolve the phase of multipotential deposited MnOx, PDF analysis revealed that the films are birnessite-like. A single phase structural model of birnessite produced low residuals in the PDF fit at low *r* range, although there were slight mismatches between the calculated and experimental PDFs at higher *r* values (Figure 14). Other single phase fits with pyrolusite (β-MnO_2), akhtenkite (ε-MnO_2), hausmannite (α-Mn_3O_4), bixbyite (α-Mn_2O_3), manganosite (MnO), rancieite ((Ca,Mn^{2+})$Mn_4^{4+}O_9 \cdot 3H_2O$), and Mn_5O_8 structures resulted in poor goodness-of-fit factors. These candidate structures were selected from active manganese oxide phases for OER reported in recent literature.[48,49,54,139] For example, the Mn_5O_8 phase seemed promising because it is a metastable phase of manganese oxide that is active for OER[139] and exhibits structural similarities with birnessite since it is comprised of sheets of edge-sharing Mn^{4+} octahedra but with Mn^{2+} between the layers. Unfortunately, PDF does not support the fit of Mn_5O_8 to activated MnOx with predicted particle sizes that are too small and poor intermediate-range agreement to activated MnOx.

Introducing a two-phase model (by varying the second phase among a number of manganese oxide polymorphs including hausmannite and bixbyite) along with a more robust optimizer algorithm did not improve the fit residuals either. Typically, the possibility of a second phase manifests as extra unfit signal in the low *r* range (such as with cathodized MnOx), since this region describes the local coordination environments of Mn and O, which would significantly differ between phases. In contrast, deviations in the model fit in the high *r* region are often associated with an inaccurate shape function or with the incorrect assumption that the model is composed of repeating structural units. For all MnOx samples, a

spherical shape function was employed to model the nanoparticulate nature of the catalyst domains, and changing the shape function to cylindrical resulted in only a negligible improvement to the fit.

Instead, the PDF of multipotential deposited MnOx was consistent with a single birnessite phase in "turbostratic disorder". This effect is commonly observed in layered materials,[140–143] such as in poorly crystalline manganese oxides including birnessite,[74,141–143] where each layer rotates or shifts relative to the adjacent one. This effect causes atomic pair distances between layers to vary, which results in the appearance of additional PDF peaks at higher *r* values. The increased disorder in multipotential deposited MnOx disrupts Bragg diffraction and explains why the XRD pattern of the sample lacks notable peaks. The 2θ = ~12° peak of birnessite, which is very prominent in as-deposited MnOx (Figure 12), corresponds to a *d*-spacing of ~7 Å based on the Bragg equation. This value agrees with the *c*-lattice parameter of the birnessite structure (i.e., the interlayer spacing). The complete loss of this peak in the XRD pattern of multipotential deposited MnOx is due to turbostratic disorder that causes the layers in birnessite to be poorly stacked.

These structural studies support a model where activated MnOx is comprised of disordered birnessite, formed by a cycle of phase conversions from ordered birnessite to hausmannite and back to disordered birnessite (Figure 18). Nanosized domains of birnessite (formed at anodic potentials) are partially converted to hausmannite at the catalyst surface by comproportionation with $Mn(OH)_2$ in solution (generated at cathodic potentials). We propose that the hausmannite layer is then transformed to turbostratic-disordered birnessite when the catalyst domains are subjected to an anodic pulse from potential cycling deposition protocols or from oxygen evolution. This disordered birnessite phase is unique in that, unlike the original ordered birnessite phase, it is more active for OER in neutral and acidic solutions.

Although redox-state cycling may improve transport properties in catalyst films,[144] the lower Tafel slopes of the disordered birnessite phase is consistent with more facile OER kinetics at active sites rather than better hole and proton transport between the electrode and active sites. Modeling transport throughout the bulk film as a series of self-exchange reactions between metal centers,[145] if the self-exchange process was turnover limiting during OER, then any film growth beyond a single monolayer should not result in additional activity. In contrast, the OER activity of MnOx increases with thicker films,[34] and no curvature of the Tafel plot to higher slopes (a possible indicator of transport limitations) is observed for activated MnOx. Similarly, the MnOx films prepared in this study were thin (estimated <50 nm by SEM) and so even assuming a worst-case resistivity for the films (e.g., 1 MΩ cm) results in through-film resistances (e.g., ~5 Ω) less than solution resistance (i.e., ~17 Ω). Tafel plots were recorded at low current densities (< 1 mA/cm^2) to minimize the effect of any uncompensated resistance, which negligible given the linearity of all Tafel plots—otherwise, significant curvature would be observed. Indeed, electrochemical impedance spectroscopy measurements comparing a blank FTO substrate to MnOx films electrodeposited on FTO estimate a negligible ~0.4 Ω of resistance through both as-deposited and activated MnOx. These control experiments further support that the lower Tafel slopes of activated MnOx are the result of improved OER kinetics.

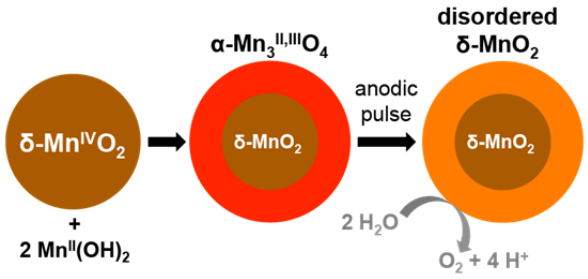

Figure 18. Schematic for the structure of nanosized MnOx domains during activation. First, birnessite (δ-MnO_2, from constant potential deposition) undergoes surface comproportionation with $Mn^{II}(OH)_2$, formed by cathodization. The resulting hausmannite (α-$Mn_3^{II,III}O_4$) then converts to disordered birnessite upon anodic conditioning (from either voltage cycling protocols or during oxygen evolution). This disordered birnessite layer is more active towards OER than the original birnessite phase.

The introduction of disordered birnessite explains why crystalline birnessite formed from chemical synthesis and annealing appears less active than birnessite prepared without annealing[43,48,54] or electrodeposited from CV cycling[47,107]. In addition, our results suggest that when lower valent manganese oxides (such as hausmannite or bixbyite) undergo OER, the samples begins to become amorphous and change into disordered birnessite, which is the actual species performing OER. Similar amorphization of crystalline MnO particles to an OER active birnessite-like phase by using a Ce^{IV} oxidant has been reported by Driess et al.[146,147] In general, many crystalline materials become disordered under anodic conditioning, with recent examples including $LiCoPO_4$,[148] Ba/Sr/Co/Fe perovskites,[149] and Co/Mn double layered hydroxides.[101]

An additional aspect of disordered birnessite is that the average Mn oxidation state is slightly lower than that of the original birnessite phase. XPS suggests that disordered birnessite contains a mixture of Mn^{4+} and Mn^{3+} valency in activated MnOx (Figure 11). X-ray absorption spectroscopy and other XPS studies on similar CV deposited manganese oxide films estimate an average oxidation state of +3.6–3.8, which is consistent with the presence of Mn^{3+}.[47,49,107] These Mn^{3+} sites are likely introduced when hausmannite is imperfectly converted to disordered birnessite. The large structural change when transforming from a spinel to a layered material is kinetically sluggish and may result in imperfections that trap Mn^{3+} species,[150] which logically comprise the resting state of highly active sites for oxygen evolution. The high spin electron configuration of Mn^{3+} is ideal for promoting fast self-exchange and labile Mn–O bonds.[34] Weakening of the metal-oxo bond can enhance OER kinetics yet retain structural stability because these Mn^{3+} sites are embedded in robust oxidic Mn^{4+} matrix.

Performance of activated MnOx in acid. Activated MnOx has a Tafel slope of ~91 mV/decade in P_i buffer at pH 2.5 (Figure 3) and represents a significant improvement over as-deposited MnOx, which exhibits a Tafel slope of ~650 mV/decade in the same conditions. At an overpotential of ~600 mV, activated MnOx is two orders of magnitude more active for OER than as-deposited MnOx, and this gap will further increase as the films are operated at higher overpotential. In addition, activated MnOx is stable in acid where films sustaining oxygen evolution in P_i at pH 2.5 and sulfuric acid at

pH 0.3 maintained low overpotentials (η = ~540 mV at 0.1 mA/cm^2) over eight hours of operation (Figure S4). For comparison at pH 2.5, unactivated MnOx and FTO require overpotentials of ~990 and ~1250 mV, respectively. In addition, activated MnOx requires only 237 mV higher potential than IrOx (at similar mass loading) to operate at 0.1 mA/cm^2 in pH 2.5 (Figure S4). These results demonstrate that activated MnOx can achieve high OER activities while retaining the acid stability of as-deposited films.

However, an inherent limitation of manganese oxide films is the phase change from MnO_2 to MnO_4^- (permanganate) that occurs at high anodic potentials and leads to dissolution of the catalyst. The potential–pH dependence of this phase conversion is governed by the Pourbaix diagram of manganese oxide.[25] In practice, there is an additional overpotential for this process due to the kinetic barrier for the $3e^-/4H^+$ MnO_2/MnO_4^- transformation. The transition between OER on MnOx to permanganate formation manifests as a distinct mechanistic change in the Tafel slope. For example at pH 2.5, the Tafel slope decreases from ~650 mV/decade (for as-deposited MnOx) to ~130 mV/decade above 1.67 V (Figure S17). Thus, all Tafel plots and stability tests in this paper were recorded at potentials with no permanganate formation. Consequently, to achieve higher current densities while maintaining long-term stability, the operating potential should be restricted while catalyst loading and electrode surface area are optimized. As a proof of concept demonstration, activated MnOx was electrodeposited on a carbon cloth substrate (with ~14 times the electrochemical surface area of FTO) to achieve stable 1 mA/cm^2 operation while remaining below potentials that form permanganate (Figure S4d). Use of highly porous electrodes with 10- to 100-fold increase in surface area over planar FTO may enable activated MnOx to operate at 1–10 mA/cm^2 while retaining stability in acid, which is a target for practical applications.

CONCLUSION

The oxygen evolution activity of electrodeposited MnOx films can be increased by changing the deposition protocol from a constant anodic potential to a voltage cycling routine (alternating between positive and negative potentials). Activated MnOx has a considerably lower Tafel slope at pH 7.0 (~70 mV/decade vs. the ~120 mV/decade of as-deposited MnOx) and pH 2.5 (~90 mV/decade vs. ~650 mV/decade of as-deposited MnOx). These lower Tafel slopes result in at least an order of magnitude increase in current density over unactivated MnOx at higher OER overpotentials, particularly in acidic solutions. The nature of the activated MnOx, as defined by the results combined from electrochemical, spectroscopic, and structural techniques, support a comproportionation-driven phase change of the original birnessite-like phase to an intermediate hausmannite-like phase during cathodic pulse sequences before transforming into a disordered birnessite phase during oxygen evolution. These results explain why different manganese oxide systems in the literature have disparate OER activity profiles—because the preparation method of the films likely introduces different oxide compositions, polymorphs, and degrees of crystallinity that affect their performance. These factors influence the catalyst's mesoscale structure, which significantly impacts their reactivity, and should be considered when designing future systems for catalysis. The performance of activated MnOx provides an inroad to developing alternatives for the best acidic OER catalysts, Ru and Ir oxides, with the benefit that MnOx avoids the use of critical elements for OER.

ASSOCIATED CONTENT

Supporting Information. This material is available free of charge via the Internet at http://pubs.acs.org.

AUTHOR INFORMATION

Corresponding Author

dnocera@fas.harvard.edu

Notes

The authors declare no competing financial interest.

ACKNOWLEDGMENT

We thank Shao-Liang Zheng and Miller Li for assistance in powder X-ray diffraction, Thomas J. Kempa for help with TEM imaging, and D. Kwabena Bediako, Andrew M. Ullman, and Chong Liu for helpful discussions. This material is based upon work supported by the U.S. Department of Energy Office of Science, Office of Basic Energy Sciences under Award Number DE-SC0009565 (DGN). SEM, TEM, and XPS were performed at Harvard University's Center for Nanoscale Systems (CNS), a member of the National Nanotechnology Infrastructure Network (NNIN), which is supported by the National Science Foundation under ECS-0335765. X-ray PDF studies were supported by the Columbia University Energy Frontier Research Center funded by the U.S. Department of Energy, Basic Energy Sciences, under Grant No. DE-SC0001085 (SJLB) and the U.S. Department of Energy Office of Science, Office of Basic Energy Sciences Energy Frontier Research Center, Center for Next Generation of Materials by Design, Award Number DE-AC36-086028308 (DGN). NSLS is supported by the U.S. Department of Energy, Basic Energy Sciences (DOE-BES) under grant DE-AC02-98CH10886.

REFERENCES

(1) Hoffert, M. I.; Caldeira, K.; Jain, A. K.; Haites, E. F.; Harvey, L. D. D.; Potter, S. D.; Schlesinger, M. E.; Schneider, S. H.; Watts, R. G.; Wigley, T. M. L.; Wuebbles, D. J. *Nature* **1998**, *395*, 881–884.

(2) Nocera, D. G. *Energy Environ. Sci.* **2010**, *3*, 993–995.

(3) Abbott, D. *Proc. IEEE* **2010**, *98*, 42–66.

(4) Chu, S.; Majumdar, A. *Nature* **2012**, *488*, 294–303.

(5) Lewis, N. S.; Nocera, D. G. *Proc. Natl. Acad. Sci. U.S.A.* **2006**, *103*, 15729–15735.

(6) Cook, T. R.; Dogutan, D. K.; Reece, S. Y.; Surendranath, Y.; Teets, T. S.; Nocera, D. G. *Chem. Rev.* **2010**, *110*, 6474–6502.

(7) Bard, A. J.; Fox, M. A. *Acc. Chem. Res.* **1995**, *28*, 141–145.

(8) Liu, F.; Concepcion, J. J.; Jurss, J. W.; Cardolaccia, T.; Templeton, J. L.; Meyer, T. J. *Inorg. Chem.* **2008**, *47*, 1727–1752.

(9) Nocera, D. G. *Inorg. Chem.* **2009**, *48*, 10001–10017.

(10) Barber, J. *Chem. Soc. Rev.* **2009**, *38*, 185–196.

(11) Pijpers, J. J. H.; Winkler; M. T.; Surendranath, Y.; Buonassisi, T.; Nocera, D. G. *Proc. Natl. Acad. Sci. U.S.A.* **2011**, *108*, 10056–10061.

(12) Young, E. R.; Costi, R.; Nocera, D. G.; Bulović, V. *Energy Environ. Sci.* **2011**, *4*, 2058–2061.

(13) Cox, C. R.; Winkler, M. T.; Pijpers, J. J. H.; Buonassisi T.; Nocera, D. G. *Energy Environ. Sci.* **2013**, *6*, 532–538.

(14) Reece, S. Y.; Hamel, J. A.; Sung, K.; Jarvi, T. D.; Esswein, A. J.; Pijpers, J. J. H.; Nocera, D. G. *Science* **2011**, *334*, 645–648.

(15) Nocera, D. G. *Acc. Chem. Res.* **2012**, *45*, 767–776.

(16) Winkler, M. T.; Cox, C. R.; Nocera, D. G.; Buonassisi, T. *Proc. Natl. Acad. Sci. U.S.A.* **2013**, *110*, E1076–E1082.

(17) Cox, C. R.; Lee, J. Z.; Nocera, D. G.; Buonassisi, T. *Proc. Natl. Acad. Sci. U.S.A.* **2014**, *111*, 14057–14061.

(18) Cristino, V.; Berardi, S.; Caramori, S.; Argazzi, R.; Carli, S.; Meda, L.; Tacca, A.; Bignozzi, C. A. *Phys. Chem. Chem. Phys.* **2013**, *15*, 13083–13092.

(19) Hu, S.; Shaner, M. R.; Beardslee, J. A.; Lichterman, M.; Brunschwig, B. S.; Lewis, N. S. *Science* **2014**, *344*, 1005–1009.

(20) Chen, Y. W.; Prange, P. D.; Dühnen, S.; Park, Y.; Gunji, M.; Chidsey, C. E. D.; McIntyre, P. C. *Nat. Mater.* **2011**, *10*, 539–544.

(21) Surendranath, Y.; Bediako, D. K.; Nocera, D. G. *Proc. Natl. Acad. Sci.* **2012**, *109*, 15617–15621.

(22) Sun, K.; Saadi, F. H.; Lichterman M. F.; Hale W. G.; Wang H. P.; Zhou, X. H.; Plymale N. T.; Omelchenko S. T.; He J. H.; Papadantonakis K. M.; Brunschwig, B. S.; Lewis, N. S. *Proc. Natl. Acad. Sci. U.S.A.* **2015**, *112*, 3612–3617.

(23) Gerischer, H. In *Solar Energy Conversion: Solid-State Physics Aspects*; Seraphin, B. O., Ed.; Topics in Applied Physics; Springer Berlin Heidelberg: Berlin, 1979; Vol. 31, pp. 115–172.

(24) Costi, R.; Young, E. R.; Bulović, V.; Nocera, D. G. *ACS Appl. Mater. Interfaces* **2013**, *5*, 2364–2367.

(25) Pourbaix, M. *Atlas of electrochemical equilibria in aqueous solutions*; 2nd ed.; National Association of Corrosion Engineers: New York, NY, 1974.

(26) Lutterman, D. A.; Surendranath, Y.; Nocera, D. G. *J. Am. Chem. Soc.* **2008**, *131*, 3838–3839.

(27) Gerken, J. B.; McAlpin, J. G.; Chen, J. Y. C.; Rigsby, M. L.; Casey, W. H.; Britt, R. D.; Stahl, S. S. *J. Am. Chem. Soc.* **2011**, *133*, 14431–14442.

(28) Esswein, A. J.; Surendranath, Y.; Reece, S. Y.; Nocera, D. G. *Energy Environ. Sci.* **2011**, *4*, 499.

(29) Surendranath, Y.; Lutterman, D. A.; Liu, Y.; Nocera, D. G. *J. Am. Chem. Soc.* **2012**, *134*, 6326–6336.

(30) Dincă, M.; Surendranath, Y.; Nocera, D. G. *Proc. Natl. Acad. Sci.* **2010**, *107*, 10337–10341.

(31) Bediako, D. K.; Surendranath, Y.; Nocera, D. G. *J. Am. Chem. Soc.* **2013**, *135*, 3662–3674.

(32) Jin, H.; Wang, J.; Su, D.; Wei, Z.; Pang, Z.; Wang, Y. *J. Am. Chem. Soc.* **2015**, *137*, 2688–2694.

(33) Huynh, M.; Bediako, D. K.; Liu, Y.; Nocera, D. G. *J. Phys. Chem. C* **2014**, *118*, 17142–17152.

(34) Huynh, M.; Bediako, D. K.; Nocera, D. G. *J. Am. Chem. Soc.* **2014**, *136*, 6002–6010.

(35) Yeo, R. S.; Orehotsky, J.; Visscher, W.; Srinivasan, S. *J. Electrochem. Soc.* **1981**, *128*, 1900–1904.

(36) Tseung, A. C. C.; Yeh, S.; Liu, X.; Kelsall, G. H.; Dykstra, P. *Novel Acid-Resistant Oxygen Evolution Electrodes*; EUR / European Commission; Commission of the European Communities: Luxembourg, 1991.

(37) Pauporté, T.; Andolfatto, F.; Durand, R. *Electrochim. Acta* **1999**, *45*, 431–439.

(38) Yagi, M.; Tomita, E.; Kuwabara, T. *J. Electroanal. Chem.* **2005**, *579*, 83–88.

(39) Reier, T.; Oezaslan, M.; Strasser, P. *ACS Catal.* **2012**, *2*, 1765–1772.

(40) Lee, Y.; Suntivich, J.; May, K. J.; Perry, E. E.; Shao-Horn, Y. *J. Phys. Chem. Lett.* **2012**, *3*, 399–404.

(41) McCrory, C. C. L.; Jung, S.; Peters, J. C.; Jaramillo, T. F. *J. Am. Chem. Soc.* **2013**, *135*, 16977–16987.

(42) Carmo, M.; Fritz, D. L.; Mergel, J.; Stolten, D. *Int. J. Hydrogen Energy* **2013**, *38*, 4901–4934.

(43) Iyer, A.; Del-Pilar, J.; King'ondu, C. K.; Kissel, E.; Garces, H. F.; Huang, H.; El-Sawy, A. M.; Dutta, P. K.; Suib., S. L. *J. Phys. Chem. C* **2012**, *116*, 6474–6483.

(44) Trotochaud, L.; Ranney, J. K.; Williams, K. N.; Boettcher, S. W. *J. Am. Chem. Soc.* **2012**, *134*, 17253–17261.

(45) Mette, K.; Bergmann, A.; Tessonnier, J.-P.; Hävecker, M.; Yao, L.; Ressler, T.; Schlögl, R.; Strasser, P.; Behrens, M. *ChemCatChem* **2012**, *4*, 851–862.

(46) Ramírez, A.; Bogdanoff, P.; Friedrich, D.; Fiechter, S. *Nano Energy* **2012**, *1*, 282–289.

(47) Zaharieva, I.; Chernev, P.; Risch, M.; Klingan, K.; Kohlhoff, M.; Fischer, A.; Dau, H. *Energy Environ. Sci.* **2012**, *5*, 7081–7089.

(48) Robinson, D. M.; Go, Y. B.; Mui, M.; Gardner, G.; Zhang, Z.; Mastrogiovanni, D.; Garfunkel, E.; Li, J.; Greenblatt, M.; Dismukes, G. C. *J. Am. Chem. Soc.* **2013**, *135*, 3494–3501.

(49) Gorlin, Y.; Lassalle-Kaiser, B.; Benck, J. D.; Gul, S.; Webb, S. M.; Yachandra, V. K.; Yano, J.; Jaramillo, T. F. *J. Am. Chem. Soc.* **2013**, *135*, 8525–8534.

(50) Fekete, M.; Hocking, R. K.; Chang, S. L. Y.; Italiano, C.; Patti, A. F.; Arena, F.; Spiccia, L. *Energy Environ. Sci.* **2013**, *6*, 2222–2232.

(51) Smith, R. D. L.; Prévot, M. S.; Fagan, R. D.; Zhang, Z.; Sedach, P. A.; Siu, M. K. J.; Trudel, S.; Berlinguette, C. P. *Science* **2013**, *340*, 60–63.

(52) Zhou, F.; Izgorodin, A.; Hocking, R. K.; Armel, V.; Spiccia, L.; Macfarlane, D. R. *ChemSusChem* **2013**, *6*, 643–651.

(53) Jin, K.; Park, J.; Lee, J.; Yang, K. D.; Pradhan, G. K.; Sim, U.; Jeong, D.; Jang, H. L.; Park, S.; Kim, D.; Sung, N.-E.; Kim, S. H.; Han, S.; Nam, K. T. *J. Am. Chem. Soc.* **2014**, *3*, 2–10.

(54) Pokhrel, R.; Goetz, M. K.; Shaner, S. E.; Wu, X.; Stahl, S. S. *J. Am. Chem. Soc.* **2015**, *137*, 8384–8387.

(55) Meng, Y.; Song, W.; Huang, H.; Ren, Z.; Chen, S.; Suib, S. L. *J. Am. Chem. Soc.* **2014**, *136*, 11452–11464.

(56) Takashima, T.; Hashimoto, K.; Nakamura, R. *J. Am. Chem. Soc.* **2012**, *134*, 1519–1527.

(57) Morita, M.; Iwakura, C.; Tamura, H. *Electrochim. Acta* **1979**, *24*, 357–362.

(58) Najafpour, M. M.; Leonard, K. C.; Fan, F.-R. F.; Tabrizi, M. A.; Bard, A. J.; King'ondu, C. K.; Suib, S. L.; Haghighi, B.; Allakhverdiev, S. I. *Dalt. Trans.* **2013**, *42*, 5085–5091.

(59) Bloor, L. G.; Molina, P. I.; Symes, M. D.; Cronin, L. *J. Am. Chem. Soc.* **2014**, *136*, 3304–3311.

(60) Krihak, M.; Murtagh, M. T.; Shahriari, M. R. *Proc. SPIE* **1996**, *2836*, 105–115.

(61) Petit, M. A.; Plichon, V. *J. Electroanal. Chem.* **1998**, *444*, 247–252.

(62) Hepel, M. In *Interfacial Electrochemistry: Theory: Experiment, and Applications*; Wieckowski, A., Ed.; Marcel Dekker, Inc.: New York, 1999; pp. 599–630.

(63) Watts, J. F.; Wolstenholme, J. *An Introduction to Surface Analysis by XPS and AES*; John Wiley & Sons, Ltd: Chichester, UK, 2003.

(64) Anthony, M. T.; Seah, M. P. *Surf. Interface Anal.* **1984**, *6*, 95–106.

(65) Barr, T. L.; Seal, S. *J. Vac. Sci. Technol. A* **1995**, *13*, 1239–1246.

(66) Ching, S.; Landrigan, J. A.; Jorgensen, M. L. *Chem. Mater.* **1995**, *7*, 1604–1606.

(67) Chupas, P. J.; Qiu, X.; Hanson, J. C.; Lee, P. L.; Grey, C. P.; Billinge, S. J. L. *J. Appl. Crystallogr.* **2003**, *36*, 1342–1347.

(68) Hammersley, A. P.; Svenson, S. O.; Hanfland, M.; Hauserman, D. *High Pressure Res.* **1996**, *14*, 235–248.

(69) Juhás, P.; Davis, T.; Farrow, C. L.; Billinge, S. J. L. *J. Appl. Crystallogr.* **2013**, *46*, 560–566.

(70) Egami, T.; Billinge, S. J. L. *Underneath the Bragg Peaks: Structural Analysis of Complex Materials*; Elsevier: Amsterdam, 2012; Vol 16.

(71) Proffen, T.; Billinge, S. J. L. *J. Appl. Crystallogr.* **1999**, *32*, 572–575.

(72) Farrow, C. L.; Juhás, P.; Liu, J. W.; Bryndin, D.; Božin, E. S.; Bloch, J.; Proffen, T.; Billinge, S. J. L. *J. Phys. Condens. Matter* **2007**, *19*, 335219–335226.

(73) Farrow, C. L.; Juhas, P.; Billinge, S. J. L. *SrFit*, 2010. http://www.diffpy.org/diffpy.srfit/ (accessed August 1, 2014).

(74) Zhu, M.; Farrow, C. L.; Post, J. E.; Livi, K. J. T.; Billinge, S. J. L.; Ginder-Vogel, M.; Sparks, D. L. *Geochim. Cosmochim. Acta* **2012**, *81*, 39–55.

(75) Farrow, C. L.; Billinge, S. J. L. *Acta Crystallogr. A.* **2009**, *65*, 232–239.

(76) Shi, C.; Redmond, E. L.; Mazaheripour, A.; Juhas, P.; Fuller, T. F.; Billinge, S. J. L. *J. Phys. Chem. C* **2013**, *117*, 7226–7230.
(77) Masadeh, A.; Božin, E.; Farrow, C.; Paglia, G.; Juhas, P.; Billinge, S.; Karkamkar, A.; Kanatzidis, M. *Phys. Rev. B* **2007**, *76*, 115413–115424.
(78) Gileadi, E. Physical Electrochemistry: Fundamentals, Techniques and Applications; 1st ed.; Wiley-VCH: Weinheim, 2011.
(79) Lyons, M. E. G.; Brandon, M. P. *Int. J. Electrochem. Sci.* **2008**, *3*, 1386–1424.
(80) Trotochaud, L.; Young, S. L.; Ranney, J. K.; Boettcher, S. W. *J. Am. Chem. Soc.* **2014**, *136*, 6744–6753.
(81) Bediako, D. K.; Li, N.; Kempa, T. J.; Nocera, D. G. *J. Am. Chem. Soc.* **2015**, submitted for publication.
(82) Burke, M. S.; Kast, M. G.; Trotochaud, L.; Smith, A. M.; Boettcher, S. W. *J. Am. Chem. Soc.* **2015**, *137*, 3638–3648.
(83) Carver, J. C.; Schweitzer, G. K.; Carlson, T. A. *J. Chem. Phys.* **1972**, *57*, 973.
(84) Oku, M.; Hirokawa, K.; Ikeda, S. *J. Electron Spectros. Relat. Phenomena* **1975**, *7*, 465–473.
(85) Rao, C. N. R.; Sarma, D. D.; Vasudevan, S.; Hegde, M. S. *Proc. R. Soc. A Math. Phys. Eng. Sci.* **1979**, *367*, 239–252.
(86) Foord, J. S.; Jackman, R. B.; Allen, G. C. *Philos. Mag. A* **1984**, *49*, 657–663.
(87) Di Castro, V.; Polzonetti, G. *J. Electron Spectros. Relat. Phenomena* **1989**, *48*, 117–123.
(88) Nesbitt, H.; Banerjee, D. *Am. Mineral.* **1998**, *83*, 305–315.
(89) Nelson, A. J.; Reynolds, J. G.; Roos, J. W. *J. Vac. Sci. Technol. A* **2000**, *18*, 1072–1076.
(90) Chigane, M.; Ishikawa, M. *J. Electrochem. Soc.* **2000**, *147*, 2246–2251.
(91) Cerrato, J. M.; Hochella, M. F.; Knocke, W. R.; Dietrich, A. M.; Cromer, T. F. *Environ. Sci. Technol.* **2010**, *44*, 5881–5886.
(92) Biesinger, M. C.; Payne, B. P.; Grosvenor, A. P.; Lau, L. W. M.; Gerson, A. R.; Smart, R. S. C. *Appl. Surf. Sci.* **2011**, *257*, 2717–2730.
(93) Galakhov, V.; Demeter, M.; Bartkowski, S.; Neumann, M.; Ovechkina, N.; Kurmaev, E.; Lobachevskaya, N.; Mukovskii, Y.; Mitchell, J.; Ederer, D. *Phys. Rev. B* **2002**, *65*, 113102.
(94) Gupta, R.; Sen, S. *Phys. Rev. B* **1975**, *12*, 15–19.
(95) Proffen, T.; Billinge, S. J. L.; Egami, T.; Louca, D. *Zeitschrift für Krist.* **2003**, *218*, 132–143.
(96) Billinge, S. J. L.; Kanatzidis, M. G. *Chem. Commun.* **2004**, 749–760.
(97) Myers, J. L.; Well, A.; Lorch, R. F. *Research Design and Statistical Analysis; 3rd ed.*; Routledge: New York, 2010.
(98) Dykhne, T.; Taylor, R.; Florence, A.; Billinge, S. J. L. *Pharm. Res.* **2011**, *28*, 1041–1048.
(99) Takashima, T.; Hashimoto, K.; Nakamura, R. *J. Am. Chem. Soc.* **2012**, *134*, 18153–18156.
(100) Singh, R.; Singh, J.; Nguyencong, H.; Chartier, P. *Int. J. Hydrogen Energy* **2006**, *31*, 1372–1378.
(101) Song, F.; Hu, X. *J. Am. Chem. Soc.* **2014**, *136*, 16481–16484.
(102) Godinho, M. I.; Catarino, M. A.; da Silva Pereira, M. I.; Mendonça, M. H.; Costa, F. M. *Electrochim. Acta* **2002**, *47*, 4307–4314.
(103) Gerken, J. B.; Chen, J. Y. C.; Massé, R. C.; Powell, A. B.; Stahl, S. S. *Angew. Chem. Int. Ed.* **2012**, *51*, 6676–6680.
(104) Kumar, M.; Awasthi, R.; Sinha, A. S. K.; Singh, R. N. *Int. J. Hydrogen Energy* **2011**, *36*, 8831–8838.
(105) Bockris, J. O.; Otagawa, T. *J. Phys. Chem.* **1983**, *87*, 2960–2971.
(106) Suntivich, J.; May, K. J.; Gasteiger, H. A.; Goodenough, J. B.; Shao-Horn, Y. *Science* **2011**, *334*, 1383–1385.
(107) Gorlin, Y.; Jaramillo, T. F. *J. Electrochem. Soc.* **2012**, *159*, H782–H786.
(108) Trasatti, S.; Petrii, O. A. *J. Electroanal. Chem.* **1992**, *327*, 353–376.
(109) Nagarajan, N.; Humadi, H.; Zhitomirsky, I. *Electrochim. Acta* **2006**, *51*, 3039–3045.
(110) Zhitomirsky, I.; Cheong, M.; Wei, J. *JOM* **2007**, *59*, 66–69.
(111) Nayak, P. K.; Munichandraiah, N. *Electrochem. Solid-State Lett.* **2009**, *12*, A115–A119.
(112) Nayak, P. K.; Devaraj, S.; Munichandraiah, N. *Electrochem. Solid-State Lett.* **2010**, *13*, F29–F32.
(113) Salyer, D.; Sweet, T. R. *Anal. Chem.* **1958**, *30*, 1632–1635.
(114) Benson, P.; Briggs, G. W. D.; Wynne-Jones, W. F. K. *Electrochim. Acta* **1964**, *9*, 275–280.
(115) Cui, C. Q.; Jiang, S. P.; Tseung, A. C. C. *J. Electrochem. Soc.* **1990**, *137*, 3418–3423.
(116) Dinamani, M.; Kamath, P. V. *J. Appl. Electrochem.* **2000**, *30*, 1157–1161.
(117) Nguyen, Q.; Wang, L.; Lu, G. M. *Int. J. Nanotechnol.* **2007**, *4*, 588–596.
(118) Amadelli, R.; Ferro, S.; Barison, S.; Kötz, R.; Schnyder, B.; Velichenko, A. B. *Electrocatalysis* **2013**, *4*, 329–337.
(119) Sonavane, A. C.; Inamdar, A. I.; Shinde, P. S.; Deshmukh, H. P.; Patil, R. S.; Patil, P. S. *J. Alloys Compd.* **2010**, *489*, 667–673.
(120) El-Sherik, A. M.; Erb, U. *J. Mater. Sci.* **1995**, *30*, 5743–5749.
(121) Carpenter, M. K.; Conell, R. S.; Corrigan, D. A. *Sol. Energy Mater.* **1987**, *16*, 333–346.
(122) Li, M.; Dincă, M. *J. Am. Chem. Soc.* **2011**, *133*, 12926–12929.
(123) Duca, M.; Koper, M. T. M. *Energy Environ. Sci.* **2012**, *5*, 9726–9742.
(124) Athouël, L.; Moser, F.; Dugas, R.; Crosnier, O.; Bélanger, D.; Brousse, T. *J. Phys. Chem. C* **2008**, *112*, 7270–7277.
(125) Sopčić, S.; Peter, R.; Petravić, M.; Mandić, Z. *J. Power Sources* **2013**, *240*, 252–257.
(126) Davies, G. *Coord. Chem. Rev.* **1969**, *4*, 199–224.
(127) Hem, J. D. *Chem. Geol.* **1978**, *21*, 199–218.
(128) Lume-Pereira, C.; Baral, S.; Henglein, A.; Janata, E. *J. Phys. Chem.* **1985**, *89*, 5772–5778.
(129) Wiechen, M.; Zaharieva, I.; Dau, H.; Kurz, P. *Chem. Sci.* **2012**, *3*, 2330–2339.
(130) Subramanian, V.; Zhu, H.; Vajtai, R.; Ajayan, P. M.; Wei, B. *J. Phys. Chem. B* **2005**, *109*, 20207–20214.
(131) Wei, W.; Cui, X.; Chen, W.; Ivey, D. G. *Chem. Soc. Rev.* **2011**, *40*, 1697–1721.
(132) Zhou, F.; Izgorodin, A.; Hocking, R. K.; Spiccia, L.; MacFarlane, D. R. *Adv. Energy Mater.* **2012**, *2*, 1013–1021.
(133) Chen, W.; Rakhi, R. B.; Wang, Q.; Hedhili, M. N.; Alshareef, H. N. *Adv. Funct. Mater.* **2014**, *24*, 3130–3143.
(134) Klug, H. P.; Alexander, L. E. X-ray diffraction procedures for polycrystalline and amorphous materials; 2nd ed.; Wiley: New York, 1974.
(135) Liu, Y.; Nocera, D. G. *J. Phys. Chem. C* **2014**, *118*, 17060–17066.
(136) Birkholz, M. *Thin Film Analysis by X-Ray Scattering*; Wiley-VCH Verlag GmbH: Weinheim, 2005.
(137) Du, P.; Kokhan, O.; Chapman, K. W.; Chupas, P. J.; Tiede, D. M. *J. Am. Chem. Soc.* **2012**, *134*, 11096–11099.
(138) Farrow, C. L.; Bediako, D. K.; Surendranath, Y.; Nocera, D. G.; Billinge, S. J. L. *J. Am. Chem. Soc.* **2013**, *135*, 6403–6406.
(139) Jeong, D.; Jin, K.; Jerng, S. E.; Seo, H.; Kim, D.; Nahm, S. H.; Kim, S. H.; Nam, K. T. *ACS Catal.* **2015**, *5*, 4624–4628.
(140) Petkov, V.; Trikalitis, P. N.; Bozin, E. S.; Billinge, S. J. L.; Vogt, T.; Kanatzidis, M. G. *J. Am. Chem. Soc.* **2002**, *124*, 10157–10162.
(141) Drits, V. A.; Lanson, B.; Gaillot, A.-C. *Am. Mineral.* **2007**, *92*, 771–788.
(142) Holland, K. L.; Walker, J. R. *Clays Clay Miner.* **1996**, *44*, 744–748.
(143) Manceau, A.; Marcus, M. A.; Grangeon, S.; Lanson, M.; Lanson, B.; Gaillot, A.-C.; Skanthakumar, S.; Soderholm, L. *J. Appl. Crystallogr.* **2013**, *46*, 193–209.
(144) Wang, H.; Lee, H.-W.; Deng, Y.; Lu, Z.; Hsu, P.-C.; Liu, Y.; Lin, D.; Cui, Y. *Nat. Commun.* **2015**, *6*, 7261.
(145) Bediako, D. K.; Costentin, C.; Jones, E. C.; Nocera, D. G.; Savéant, J. *J. Am. Chem. Soc.* **2013**, *135*, 10492–10502.
(146) Indra, A.; Menezes, P. W.; Zaharieva, I.; Baktash, E.; Pfrommer, J.; Schwarze, M.; Dau, H.; Driess, M. *Angew. Chem. Int. Ed.* **2013**, *52*, 13206–13210.

(147) Indra, A.; Menezes, P. W.; Ranjbar Sahraie, N.; Bergmann, A.; Das, C.; Tallarida, M.; Schmeißer, D.; Strasser, P.; Driess, M. *J. Am. Chem. Soc.* **2014**, doi: 10.1021/ja509348t.

(148) Lee, S. W.; Carlton, C.; Risch, M.; Surendranath, Y. Chen, S.; Furutsuki, S.; Yamada, A.; Nocera, D. G.; Shao–Horn, Y. *J. Am. Chem. Soc.* **2012**, *134*, 16959–16962.

(149) May, K. J.; Carlton, C. E.; Stoerzinger, K. A.; Risch, M.; Suntivich, J.; Lee, Y.; Grimaud, A.; Shao-Horn, Y. *J. Phys. Chem. Lett.* **2012**, *3*, 3264–3270.

(150) Li, Y.; Bareñoa, J.; Bettgea, M.; Abrahama, D. P. *J. Electrochem. Soc.* **2015**, *162*, A155–A161.

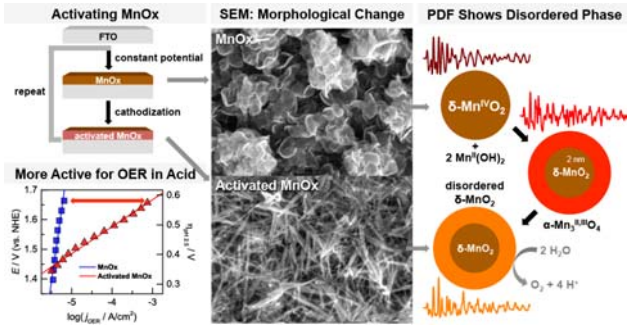
Activating MnOx
FTO
constant potential
MnOx
repeat
cathodization
activated MnOx
More Active for OER in Acid
MnOx
Activated MnOx
SEM: Morphological Change
MnOx
Activated MnOx
PDF Shows Disordered Phase
δ-Mn^IVO2
2 Mn^II(OH)2
2 nm
δ-MnO2
disordered
δ-MnO2
α-Mn3^II,III O4
δ-MnO2
2 H2O
O2 + 4 H+